PARAMETRIC RESONANCE IN SPHERICAL IMMERSED ELASTIC SHELLS*

WILLIAM KO† AND JOHN M. STOCKIE†

Abstract. We perform a stability analysis for a fluid-structure interaction (FSI) problem in which a spherical elastic shell or membrane is immersed in a 3D viscous, incompressible fluid. The shell is an idealized structure having zero thickness, and has the same fluid lying both inside and outside. The problem is formulated mathematically using the immersed boundary framework in which Dirac delta functions are employed to capture the two-way interaction between fluid and immersed structure. The elastic structure is driven parametrically via a time-periodic modulation of the elastic membrane stiffness. We perform a Floquet stability analysis in the case of both a viscous and inviscid fluid, and demonstrate that the forced fluid-membrane system gives rise to parametric resonances in which the solution becomes unbounded even in the presence of viscosity. The analytical results are validated using numerical simulations with a 3D immersed boundary code for a range of wavenumbers and physical parameter values. Moreover, we propose a benchmark computation that is supported by our analytical results and which other FSI software developers can use to validate their simulations. Finally, potential applications to biological systems are discussed, with a particular focus on the human heart and investigating whether or not FSI-mediated instabilities could play a role in cardiac fluid dynamics.

Key words. elastic membranes, parametric forcing, Floquet stability analysis, immersed boundary method.

AMS subject classifications. 70K28, 74F10, 76D05, 76Z05.

1. Introduction.

Fluid-structure interaction (or FSI) problems are ubiquitous in scientific and industrial applications. Because of the complex coupling that occurs between the fluid and moving structure, FSI problems present formidable challenges to both mathematical modelers and computational scientists. Of particular interest in this paper are flows involving a highly deformable elastic structure immersed in a viscous fluid, which is common in biofluid systems such as blood flow in the heart or arteries, dynamics of swimming or flying organisms, and organ systems [19, 26, 38].

One approach that has proven particularly effective at capturing FSI with highly deformable structures is the immersed boundary (or IB) method [32]. This approach was initially developed by Peskin [31] to study the flow of blood in a beating heart, and has since been employed in a wide range of biological and industrial applications. The primary advantage of the IB method is its ability to capture the full two-way interaction between an elastic structure and a surrounding fluid in a simple manner using Dirac delta function source terms, which also leads to a simple and efficient numerical implementation.

A common test problem that is often employed to validate mathematical models and numerical algorithms for FSI problems involves an oscillating spherical elastic shell immersed in fluid, very much like a rubber water balloon immersed in a water-filled container. The 2D analogue of this problem is the standard circular membrane problem that pervades the IB literature. Extensive research has also been performed on numerical simulations of immersed spherical shells that aims to develop accurate and efficient algorithms, with applications ranging from red blood cell deformation [34], to sound propagation in the cochlea [11], to contraction of cell membranes [8].

Apart from numerical simulations, relatively little mathematical analysis has been performed on such FSI problems owing to the complex nonlinear coupling between the equations governing the elastic structure and the fluid in which it is immersed. Stockie and Wetton [36] performed a linear stability analysis of the IB model in two dimensions for a simple geometry in which a flat membrane or sheet is immersed in fluid. They also presented asymptotic results on the frequency and rate of decay of membrane oscillations that depends on the wavenumber of the sinusoidal perturbation, as well as validating their analytical results using immersed boundary simulations. Cortez and Varela [7] performed a nonlinear analysis of a perturbed circular elastic membrane immersed in an inviscid fluid. These results were later extended by Cortez et al. [6] to the study of parametric instabilities of an internally-forced elastic membrane in two dimensions, in which the forcing appears as a periodic modulation of the elastic stiffness parameter. These authors showed that such systems can give rise to parametric resonance, which overcomes viscous fluid damping and thereby causes the elastic structure to become unstable. A similar analysis was performed by Ko and Stockie [21] for a simpler 2D flat-membrane geometry, who

* Financial support for this work came from a Discovery Grant and a Discovery Accelerator Award from the Natural Sciences and Engineering Research Council of Canada.

†Department of Mathematics, Simon Fraser University, 8888 University Drive, Burnaby, BC, V5A 1S6, Canada (wka11@sfu.ca, jstockie@sfu.ca).

applied their results to the study of internally-forced oscillations in the mammalian cochlea. Parametric resonance is a generic form of unstable response that can arise whenever there is a time-periodic variation in a system parameter [5], and such resonances have been identified in a wide range of other fluid and biofluid systems, for example [13, 18, 23, 35].

In this article, we extend the work of Cortez et al. [6] to three dimensions by studying parametric instabilities of an elastic spherical shell immersed in a incompressible, Newtonian fluid. The internal forcing is induced by a time-periodic modulation of the membrane stiffness parameter. The most closely-related study in the literature is a paper by Felderhof [10] that investigates the response of an elastic shell to an impulsive acoustic forcing, which differs significantly in that it is not only an externally forced problem but also involves much more energetic excitations at much higher frequencies. Our work is motivated in part by IB models of active biological systems such as the heart, wherein the contraction and relaxation of heart muscles can be mimicked by a time-dependent muscle stiffness. Although Cottet and Maitre [9] presented some computational evidence for the existence of parametric instabilities, no analysis has yet been done of the complete three-dimensional governing equations to confirm the presence of these instabilities.

2. Problem formulation.

2.1. Immersed boundary model. We consider a closed elastic membrane that encompasses a region of viscous incompressible fluid, and is immersed in an infinite domain containing the same fluid. At equilibrium, an unforced membrane takes the form of a pressurized sphere with radius R and centered at the origin. Considering the geometry of this equilibrium state, it is natural to formulate the governing equations in spherical coordinates (r, θ, ϕ), where $r \in [0, \infty)$ is the distance from the origin, $\theta \in [0, 2\pi)$ is the azimuth angle in the horizontal plane, and $\phi \in [0, \pi]$ is the polar angle measured downward from the vertical or z-axis. The fluid motion is then described by the incompressible Navier-Stokes equations

$$\rho\left(\frac{\partial \boldsymbol{u}}{\partial t} + \boldsymbol{u}\cdot\nabla\boldsymbol{u}\right) = -\nabla p + \mu\Delta\boldsymbol{u} + \boldsymbol{f}, \tag{2.1}$$

$$\nabla\cdot\boldsymbol{u} = 0, \tag{2.2}$$

where ρ is fluid density and μ is dynamic viscosity, both assumed constant. The membrane moves with the local fluid velocity according to

$$\frac{\partial \boldsymbol{X}}{\partial t} = \boldsymbol{u}(\boldsymbol{X}, t), \tag{2.3}$$

where $\boldsymbol{X}(\xi, \eta, t)$ represents the configuration of the immersed surface, parameterized by Lagrangian coordinates $\xi \in [0, 2\pi)$ and $\eta \in [0, \pi]$.

An external force acts on the fluid due to the presence of the elastic membrane

$$\boldsymbol{f}(\boldsymbol{x}, t) = \int_0^{\pi}\int_0^{2\pi} \boldsymbol{F}(\boldsymbol{X}, t)\,\delta(\boldsymbol{x} - \boldsymbol{X})\sin\eta\,\mathrm{d}\xi\,\mathrm{d}\eta, \tag{2.4}$$

and is written in terms of a force density $\boldsymbol{F}(\boldsymbol{X}, t)$ that is integrated against the Dirac delta function. The resulting force is singular and is supported only on the membrane locations. The force density may be expressed as the variational derivative of a membrane elastic energy functional $E(\boldsymbol{X}, t)$ [32]

$$\boldsymbol{F}(\boldsymbol{X}, t) = -\frac{\wp E}{\wp \boldsymbol{X}},$$

where we have used $\wp$ to denote the variation of a functional instead of the more conventional δ to avoid confusion with the Dirac delta function. In the interests of simplicity, we choose an energy functional that incorporates membrane stretching but ignores any resistance to shearing or bending:

$$E(\boldsymbol{X}, t) = \frac{1}{2}K(t)\int_0^{\pi}\int_0^{2\pi}\left(\left\|\frac{1}{\sin\eta}\frac{\partial \boldsymbol{X}}{\partial \xi}\right\|^2 + \left\|\frac{\partial \boldsymbol{X}}{\partial \eta}\right\|^2\right)\sin\eta\,\mathrm{d}\xi\,\mathrm{d}\eta.$$

This functional describes a membrane that would shrink to a point in the absence of fluid in the interior, but when filled with fluid has a circular equilibrium state in which the fluid pressure and membrane

force balance each other. This choice was motivated by Terzopoulos and Fleischer [37] who simulated deformable sheets in computer graphics applications, and is also a simplified version of other energy functionals used in fluid-structure interaction problems [16].

Central to this paper is the specification of the periodically-varying stiffness

$$K(t) = \sigma\big(1 + 2\tau \sin(\omega t)\big), \tag{2.5}$$

where σ is an elastic stiffness parameter, ω is the forcing frequency and τ is the forcing amplitude. We restrict the amplitude to $0 \leqslant \tau \leqslant \frac{1}{2}$, corresponding to a membrane that resists stretching but not compression. The IB force density may then be written as

$$\boldsymbol{F}(\boldsymbol{X}, t) = K(t)\Delta_\xi \boldsymbol{X}, \tag{2.6}$$

where

$$\Delta_\xi = \frac{1}{\sin^2\eta}\frac{\partial^2}{\partial \xi^2} + \frac{1}{\sin\eta}\frac{\partial}{\partial\eta}\left(\sin\eta\,\frac{\partial}{\partial\eta}\right) \tag{2.7}$$

denotes the angular Laplacian operator in Lagrangian coordinates.

2.2. Nondimensionalization. To simplify the model and the analysis, we first nondimensionalize the governing equations by introducing the following re-scaled variables

$$\boldsymbol{x} = R\,\widetilde{\boldsymbol{x}}, \quad \boldsymbol{X} = R\,\widetilde{\boldsymbol{X}}, \quad t = \frac{1}{\omega}\,\widetilde{t}, \quad \boldsymbol{u} = U_c\,\widetilde{\boldsymbol{u}}, \quad p = P_c\,\widetilde{p}, \tag{2.8}$$

where tildes denote dimensionless quantities and the characteristic velocity and pressure scales are

$$U_c = R\omega \qquad \text{and} \qquad P_c = \rho R^2\omega^2.$$

Substituting the above expressions into equations (2.1)–(2.6) yields

$$\frac{\partial \widetilde{\boldsymbol{u}}}{\partial \widetilde{t}} + \widetilde{\boldsymbol{u}}\cdot\widetilde{\nabla}\widetilde{\boldsymbol{u}} = -\widetilde{\nabla}\widetilde{p} + \nu\widetilde{\Delta}\widetilde{\boldsymbol{u}} + \widetilde{\boldsymbol{f}}, \tag{2.9a}$$

$$\widetilde{\nabla}\cdot\widetilde{\boldsymbol{u}} = 0, \tag{2.9b}$$

$$\frac{\partial \widetilde{\boldsymbol{X}}}{\partial \widetilde{t}} = \widetilde{\boldsymbol{u}}(\widetilde{\boldsymbol{X}}, \widetilde{t}), \tag{2.9c}$$

$$\widetilde{\boldsymbol{f}}(\widetilde{\boldsymbol{x}}, \widetilde{t}) = \int_0^\pi\!\!\int_0^{2\pi} \widetilde{\boldsymbol{F}}(\widetilde{\boldsymbol{X}}, \widetilde{t})\,\widetilde{\delta}(\widetilde{\boldsymbol{x}} - \widetilde{\boldsymbol{X}})\sin\eta\;\mathrm{d}\xi\;\mathrm{d}\eta, \tag{2.9d}$$

$$\widetilde{\boldsymbol{F}}(\widetilde{\boldsymbol{X}}, \widetilde{t}) = \widetilde{K}(\widetilde{t})\Delta_\xi\widetilde{\boldsymbol{X}}, \tag{2.9e}$$

$$\widetilde{K}(\widetilde{t}) = \kappa(1 + 2\tau\sin\widetilde{t}), \tag{2.9f}$$

where we have introduced a dimensionless viscosity (or reciprocal Reynolds number)

$$\nu = \frac{\mu}{\rho R^2\omega} = \frac{1}{Re}, \tag{2.10}$$

and a dimensionless IB stiffness parameter

$$\kappa = \frac{\sigma}{\rho R^3\omega^2}. \tag{2.11}$$

From this point onward, the tildes are omitted from all variables. In the next two sections we perform a number of simplifications to the governing equations that make them more amenable to Floquet analysis by: (a) linearizing the equations; (b) expanding the solution in terms of vector spherical harmonics; and (c) eliminating the delta function forcing term in lieu of suitable jump conditions across the membrane.

2.3. Linearized vector spherical harmonic expansion. Consider a membrane whose shape is a perturbation of the spherical equilibrium configuration

$$\boldsymbol{X}(\xi,\eta,0) = \big(1+\epsilon g(\xi,\eta)\big)\,\hat{\boldsymbol{r}}(\xi,\eta),$$

where $\hat{\boldsymbol{r}}$ is the radial unit vector and $|\epsilon| \ll 1$ is a perturbation parameter. The equilibrium state is

$$\boldsymbol{u}_0 = \boldsymbol{0}, \qquad \boldsymbol{X}_0 = \hat{\boldsymbol{r}}, \qquad p_0 = 2K(t)\,H(1-r) + p_a,$$

where $H(r)$ is the Heaviside step function and p_a is some constant ambient pressure. We assume a solution in the form of a regular perturbation expansion

$$\begin{aligned}\boldsymbol{u} &= \boldsymbol{u}_0 + \epsilon\boldsymbol{u}_1 + O(\epsilon^2),\\ \boldsymbol{X} &= \boldsymbol{X}_0 + \epsilon\boldsymbol{X}_1 + O(\epsilon^2),\\ p &= p_0 + \epsilon p_1 + O(\epsilon^2).\end{aligned}$$

Substituting these expressions into the governing equations and retaining only those terms of $O(\epsilon)$, we obtain the following system for the first-order quantities:

$$\frac{\partial \boldsymbol{u}_1}{\partial t} = -\nabla p_1 + \nu\Delta\boldsymbol{u}_1 + \boldsymbol{f}_1, \tag{2.12a}$$

$$\nabla\cdot\boldsymbol{u}_1 = 0, \tag{2.12b}$$

$$\frac{\partial \boldsymbol{X}_1}{\partial t} = \boldsymbol{u}_1(\boldsymbol{X}_0, t). \tag{2.12c}$$

The stability of the fluid-membrane system may then be determined by studying solutions of this simpler linear system for the $O(\epsilon)$ variables. Because of the symmetry in the problem we look for solutions in terms of spherical harmonics, which are eigenfunctions of the angular Laplacian operator Δ_ξ and form an orthonormal basis for sufficiently smooth functions of (ξ,η). The normalized scalar spherical harmonic of degree m and order k is

$$Y_{m,k}(\theta,\phi) = (-1)^k\sqrt{\frac{2m+1}{4\pi}\frac{(m-k)!}{(m+k)!}}\;e^{\mathrm{i}k\theta}\,P_m^k(\cos\phi), \tag{2.13}$$

where P_m^k denotes the associated Legendre polynomial [1]. The natural generalization to vector-valued functions (in our case, the fluid velocity and IB position) are *vector spherical harmonics or VSH*, for which various definitions have been proposed in the literature [3, 14, 15, 17]. For example, writing the velocity perturbation $\boldsymbol{u}_1$ in terms of the VSH proposed by Hill [15] has the advantage that it fully decouples the linearized unsteady Stokes equations in (2.12a). However, using Hill's basis in the present context would lead to significant complications later in our analysis. Therefore, we instead use the VSH basis of Barrera et al. [3] that is defined in terms of scalar spherical harmonics (2.13) as follows:

$$\begin{aligned}\boldsymbol{Y}_{m,k}(\theta,\phi) &= Y_{m,k}\,\hat{\boldsymbol{r}},\\ \boldsymbol{\Psi}_{m,k}(\theta,\phi) &= r\,\nabla Y_{m,k} = \frac{\mathrm{i}k}{\sin\phi}\,Y_{m,k}\hat{\boldsymbol{\theta}} + \frac{\partial Y_{m,k}}{\partial\phi}\,\hat{\boldsymbol{\phi}},\\ \boldsymbol{\Phi}_{m,k}(\theta,\phi) &= \hat{\boldsymbol{r}}\times\boldsymbol{\Psi}_{m,k} = \frac{\partial Y_{m,k}}{\partial\phi}\,\hat{\boldsymbol{\theta}} - \frac{\mathrm{i}k}{\sin\phi}Y_{m,k}\,\hat{\boldsymbol{\phi}},\end{aligned}$$

where $\hat{\boldsymbol{\theta}}$ and $\hat{\boldsymbol{\phi}}$ are the angular unit vectors in spherical coordinates. This choice of basis re-introduces a coupling in the momentum equations but we will see later on that it has the major advantage of decoupling the jump conditions. Furthermore, this basis decomposes vectors into a radial component and two tangential components, which provides a more intuitive geometric interpretation of our results. Finally, we only require the real part of the solution modes so that, without loss of generality, we can write the velocity, IB position and pressure variables as

$$\begin{aligned}\boldsymbol{u}_1 &= u^r(r,t)\boldsymbol{Y}^c_{m,k} + u^\Psi(r,t)\boldsymbol{\Psi}^c_{m,k} + u^\Phi(r,t)\boldsymbol{\Phi}^c_{m,k},\\ \boldsymbol{X}_1 &= X^r(t)\boldsymbol{Y}^c_{m,k} + X^\Psi(t)\boldsymbol{\Psi}^c_{m,k} + X^\Phi(t)\boldsymbol{\Phi}^c_{m,k},\\ p_1 &= \hat{p}(r,t)Y^c_{m,k},\end{aligned}$$

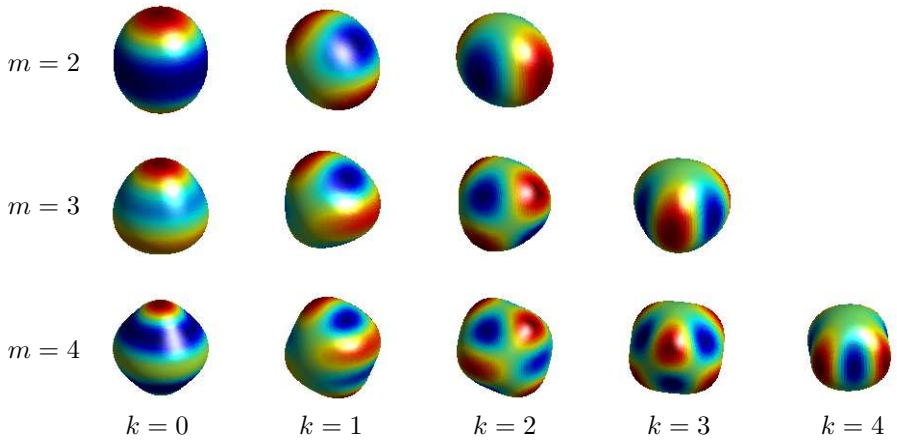

FIG. 1. *Spherical shells perturbed by a spherical harmonic mode (real part) with nonnegative order k.*

where the superscript c denotes the real (cosine) part of each spherical harmonic.

We then take an initial membrane configuration of the form

$$\boldsymbol{X}(\xi, \eta, 0) = \big(1 + \epsilon Y^c_{m,k}(\xi, \eta)\big)\hat{\boldsymbol{r}}(\xi, \eta),$$

and examine the stability of each (m, k)-mode. Several possible membrane configurations corresponding to spherical harmonics are illustrated in figure 1. Note that $m = 0$ corresponds to a radially expanding membrane, which is forbidden due to fluid incompressibility. Moreover, $m = 1$ is a simple translation of the membrane for which the system remains in equilibrium. Therefore we are only concerned with modes with $m \geq 2$ that give rise to nontrivial deformations.

2.4. Jump condition formulation. We next reformulate the equations by eliminating the delta function forcing term and replacing it with suitable jump conditions across the membrane, following the approach used by Lai and Li [24]. We first observe that equation (2.3) is a statement that the membrane must move with the local fluid velocity. Because the membrane is infinitesimally thin, the velocity must be continuous across the membrane, which leads immediately to the first jump condition

$$[\![\boldsymbol{u}_1]\!] = \boldsymbol{0}, \tag{2.14}$$

where $[\![\cdot]\!]$ denotes the jump in a quantity across the membrane Γ, or more precisely

$$[\![\cdot]\!] := \lim_{\varrho \to 0} \big((\cdot)|_{\boldsymbol{x}^+} - (\cdot)|_{\boldsymbol{x}^-}\big),$$

where we have introduced a thin region $\Omega_\varrho(t)$ surrounding Γ that extends a distance ϱ outwards from either side of the membrane, with inner surface $\partial\Omega^-_\varrho(t)$ and outer surface $\partial\Omega^+_\varrho(t)$. The jump in a quantity at location $\boldsymbol{x} \in \Gamma$ is the difference between values at $\boldsymbol{x}^+ \in \partial\Omega^+_\varrho(t)$ and $\boldsymbol{x}^- \in \partial\Omega^-_\varrho(t)$, taken in the limit as $\varrho \to 0$ where both $\boldsymbol{x}^+, \boldsymbol{x}^- \to \boldsymbol{x}$. Next, consider the divergence condition (2.9b) which must be satisfied identically on either side of the membrane so that

$$[\![\nabla \cdot \boldsymbol{u}_1]\!] = 0. \tag{2.15}$$

Rewriting this condition in terms of the components of $\boldsymbol{u}_1$, we have

$$\left[\!\!\left[\frac{\partial u^r}{\partial r} + \frac{2}{r}\, u^r - \frac{m(m+1)}{r}\, u^\Psi \right]\!\!\right] = \left[\!\!\left[\frac{\partial u^r}{\partial r} \right]\!\!\right] = 0, \tag{2.16}$$

where the last equality follows from (2.14).

The remaining jump conditions are derived from the momentum equations (2.9a). Letting $\varphi(\boldsymbol{x})$ be a smooth test function with compact support, we multiply the momentum equations by $\varphi(\boldsymbol{x})$ and integrate over $\Omega_\varrho(t)$ to obtain

$$\int_{\Omega_\varrho(t)} \left(\frac{\partial \boldsymbol{u}}{\partial t} + \boldsymbol{u} \cdot \nabla \boldsymbol{u} \right) \varphi(\boldsymbol{x})\, \mathrm{d}V = \int_{\Omega_\varrho(t)} \left(-\nabla p + \nu \Delta \boldsymbol{u} + \boldsymbol{f}\right) \varphi(\boldsymbol{x})\, \mathrm{d}V. \tag{2.17}$$

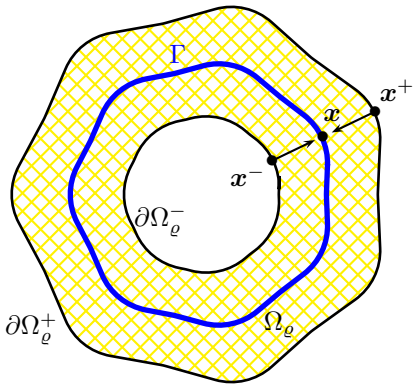

FIG. 2. *A 2D cross-sectional view of the 3D membrane* Γ *and subdomain* $\Omega_\varrho(t)$*, having inner and outer surfaces* $\partial\Omega_\varrho^-(t)$ *and* $\partial\Omega_\varrho^+(t)$ *respectively, which illustrates the limiting process as* $\boldsymbol{x}^+, \boldsymbol{x}^- \to \boldsymbol{x}$ *and* $\varrho \to 0$*.*

Following the same procedure as in [24], we arrive at the following limits as $\varrho \to 0$

$$\int_{\Omega_\varrho(t)} \left(\frac{\partial \boldsymbol{u}}{\partial t} + \boldsymbol{u}\cdot\nabla\boldsymbol{u}\right)\varphi(\boldsymbol{x})\,\mathrm{d}V \quad \to \quad 0, \tag{2.18}$$

$$\int_{\Omega_\varrho(t)} -\nabla p\,\varphi(\boldsymbol{x})\,\mathrm{d}V \quad \to \quad -\int_\Gamma [\![p]\!]\,\hat{\boldsymbol{n}}\,\varphi(\boldsymbol{X})\,\mathrm{d}A, \tag{2.19}$$

$$\int_{\Omega_\varrho(t)} \nu\Delta\boldsymbol{u}\,\varphi(\boldsymbol{x})\,\mathrm{d}V \quad \to \quad \int_\Gamma \nu[\![\hat{\boldsymbol{n}}\cdot\nabla\boldsymbol{u}]\!]\,\varphi(\boldsymbol{X})\,\mathrm{d}A, \tag{2.20}$$

where

$$\hat{\boldsymbol{n}} = \frac{\frac{\partial \boldsymbol{X}}{\partial\eta}\times\frac{\partial \boldsymbol{X}}{\partial\xi}}{\left\|\frac{\partial \boldsymbol{X}}{\partial\eta}\times\frac{\partial \boldsymbol{X}}{\partial\xi}\right\|}, \tag{2.21}$$

is the unit outward normal vector. Finally, we consider the forcing term in (2.17) and apply the sifting property of the Dirac delta function to obtain

$$\int_{\Omega_\varrho(t)} \boldsymbol{f}\varphi(\boldsymbol{x})\,\mathrm{d}V = \int_0^\pi\int_0^{2\pi} \boldsymbol{F}\,\varphi(\boldsymbol{X})\sin\eta\,\mathrm{d}\xi\,\mathrm{d}\eta. \tag{2.22}$$

The results in (2.18)–(2.20) and (2.22) can then be substituted into (2.17), after which we take the limit as $\varrho \to 0$ to get

$$0 = \int_0^\pi\int_0^{2\pi}\left(-[\![p]\!]\hat{\boldsymbol{n}}\left\|\frac{\partial \boldsymbol{X}}{\partial\eta}\times\frac{\partial \boldsymbol{X}}{\partial\xi}\right\|\frac{1}{\sin\eta} + \nu[\![\hat{\boldsymbol{n}}\cdot\nabla\boldsymbol{u}]\!]\left\|\frac{\partial \boldsymbol{X}}{\partial\eta}\times\frac{\partial \boldsymbol{X}}{\partial\xi}\right\|\frac{1}{\sin\eta} + \boldsymbol{F}\right)\varphi(\boldsymbol{X})\sin\eta\,\mathrm{d}\xi\,\mathrm{d}\eta,$$

where we have also made use of the identity for the area element

$$dA = \left\|\frac{\partial \boldsymbol{X}}{\partial\eta}\times\frac{\partial \boldsymbol{X}}{\partial\xi}\right\|\,\mathrm{d}\xi\,\mathrm{d}\eta.$$

Because φ is arbitrary and smooth, the integrand must be identically zero, which yields

$$0 = -[\![p]\!]\left(\frac{\partial \boldsymbol{X}}{\partial\eta}\times\frac{\partial \boldsymbol{X}}{\partial\xi}\right) + \nu\left[\!\!\left[\left(\frac{\partial \boldsymbol{X}}{\partial\eta}\times\frac{\partial \boldsymbol{X}}{\partial\xi}\right)\cdot\nabla\boldsymbol{u}\right]\!\!\right] + \boldsymbol{F}\sin\eta, \tag{2.23}$$

where the normal vector has been replaced using (2.21). We now make use of the perturbation expansion for $\boldsymbol{X}$ to write the terms arising from the normal vector as

$$\frac{1}{\sin\eta}\frac{\partial \boldsymbol{X}}{\partial\eta}\times\frac{\partial \boldsymbol{X}}{\partial\xi} = \hat{r} + \epsilon\Big[(2X^r - m(m+1)X^\Psi)\boldsymbol{Y}^c_{m,k} + (X^\Psi - X^r)\boldsymbol{\Psi}^c_{m,k} + X^\Phi\boldsymbol{\Phi}^c_{m,k}\Big] + O(\epsilon^2).$$

Similarly, the force density can be expanded as

$$\boldsymbol{F} = -2K(t)\hat{r} + \epsilon K(t)\Big[\left(2m(m+1)X^{\Psi} - (m^2+m+2)X^r\right)\boldsymbol{Y}^c_{m,k} + \left(2X^r - m(m+1)X^{\Psi}\right)\boldsymbol{\Psi}^c_{m,k} - m(m+1)X^{\Phi}\boldsymbol{\Phi}^c_{m,k}\Big] + O(\epsilon^2).$$

The remaining jump conditions are obtained by substituting these last two equations along with the perturbation expansions for $\boldsymbol{u}$ and p into (2.23). The radial component of (2.23) gives two jump conditions for the pressure variables

$$[\![p_0]\!] = -2K(t), \tag{2.24}$$

$$[\![p_1]\!] = -K(t)(m-1)(m+2)X^r Y^c_{m,k}, \tag{2.25}$$

while the $\boldsymbol{\Psi}_{m,k}$ and $\boldsymbol{\Phi}_{m,k}$ components give jump conditions for the radial derivatives of u^{Ψ} and u^{Φ} as

$$\nu\left[\!\!\left[\frac{\partial u^{\Psi}}{\partial r}\right]\!\!\right] = K(t)(m-1)(m+2)X^{\Psi}, \tag{2.26}$$

$$\nu\left[\!\!\left[\frac{\partial u^{\Phi}}{\partial r}\right]\!\!\right] = K(t)(m-1)(m+2)X^{\Phi}. \tag{2.27}$$

Note that the right-hand sides of each jump condition are completely decoupled, which is the major advantage to the particular choice of VSH basis that we made earlier in section 2.3.

We can now summarize the equations that will be analyzed in the remainder of this paper:

$$\frac{\partial u^r}{\partial t} = -\frac{\partial \hat{p}}{\partial r} + \nu\left(\frac{1}{r^2}\frac{\partial}{\partial r}\left(r^2\frac{\partial u^r}{\partial r}\right) - \frac{m(m+1)}{r^2}u^r - \frac{2}{r^2}u^r + \frac{2m(m+1)}{r^2}u^{\Psi}\right), \tag{2.28}$$

$$\frac{\partial u^{\Psi}}{\partial t} = -\frac{\hat{p}}{r} + \nu\left(\frac{1}{r^2}\frac{\partial}{\partial r}\left(r^2\frac{\partial u^{\Psi}}{\partial r}\right) - \frac{m(m+1)}{r^2}u^{\Psi} + \frac{2}{r^2}u^r\right), \tag{2.29}$$

$$\frac{\partial u^{\Phi}}{\partial t} = \nu\left(\frac{1}{r^2}\frac{\partial}{\partial r}\left(r^2\frac{\partial u^{\Phi}}{\partial r}\right) - \frac{m(m+1)}{r^2}u^{\Phi}\right), \tag{2.30}$$

$$\nabla\cdot\boldsymbol{u}_1 = \left(\frac{1}{r^2}\frac{\partial}{\partial r}(r^2u^r) - \frac{m(m+1)}{r}u^{\Psi}\right)Y^c_{m,k} = 0, \tag{2.31}$$

$$\frac{\partial \boldsymbol{X}_1}{\partial t} = \boldsymbol{u}_1|_{r=1}. \tag{2.32}$$

The $O(\epsilon)$ quantities $\boldsymbol{X}_1$, $\boldsymbol{u}_1$ and p_1 are also subject to the jump conditions (2.14), (2.16) and (2.25)–(2.27). Note that the $\boldsymbol{\Phi}_{m,k}$ component is completely decoupled in the momentum equations and jump conditions, which is major advantage of our choice of VSH basis; furthermore, it is not driven by a pressure gradient and so evolves independently from the other two components. In particular, if the $\boldsymbol{\Phi}_{m,k}$ component of the initial membrane position is zero, then it remains zero for all time. Hence, investigating stability of a parametrically-forced elastic shell requires only that we consider the $\boldsymbol{Y}_{m,k}$ and $\boldsymbol{\Psi}_{m,k}$ solution components. We also observe that the dynamics of the linearized solution depend only on the degree m of the spherical harmonic and not on the order k; hence, solution modes are characterized by a single integer m.

In the remainder of this paper, we will drop the subscript "1" that until now has distinguished the $O(\epsilon)$ quantities.

3. Floquet analysis for an inviscid fluid. To provide some insight into FSI-mediated parametric instabilities, we first consider a simpler version of the immersed spherical membrane problem in

which the fluid is inviscid and the governing equations reduce to

$$\frac{\partial u^r}{\partial t} = -\frac{\partial \hat{p}}{\partial r}, \tag{3.1a}$$

$$\frac{\partial u^\Psi}{\partial t} = -\frac{\hat{p}}{r}, \tag{3.1b}$$

$$\nabla \cdot \boldsymbol{u} = 0, \tag{3.1c}$$

$$\frac{\mathrm{d}X^r}{\mathrm{d}t} = u^r(1,t), \tag{3.1d}$$

$$[\![u^r]\!] = 0, \tag{3.1e}$$

$$[\![\hat{p}]\!] = -K(t)(m-1)(m+2)X^r. \tag{3.1f}$$

Note that in the absence of viscosity, it is only possible to impose the zero normal flow condition (3.1d) on the membrane instead of the usual no-slip condition.

We begin by solving for the pressure away from the membrane, which satisfies

$$\Delta p = \left(r^2 \frac{\partial^2 \hat{p}}{\partial r^2} + 2r \frac{\partial \hat{p}}{\partial r} - m(m+1)\hat{p} \right) Y^c_{m,k} = 0 \tag{3.2}$$

on either side. Imposing that the pressure be bounded when both $r = 0$ and $r \to \infty$ yields

$$\hat{p}(r,t) = \begin{cases} a(t)\, r^m, & \text{if } r < 1, \\ b(t)\, r^{-m-1}, & \text{if } r > 1, \end{cases}$$

where $a(t)$ and $b(t)$ are as-yet undetermined functions of time. Substituting this pressure solution into the inviscid momentum equation (3.1a) yields an equation for the radial fluid acceleration

$$\frac{\partial u^r}{\partial t} = \begin{cases} -ma(t)\, r^{m-1}, & \text{if } r < 1, \\ (m+1)b(t)\, r^{-m-2}, & \text{if } r > 1. \end{cases}$$

Since fluid cannot penetrate the membrane, the radial acceleration of both fluid and membrane must match and

$$\frac{\mathrm{d}^2 X^r}{\mathrm{d}t^2} = \left. \frac{\partial u^r}{\partial t} \right|_{r=1} = -ma(t) = (m+1)b(t), \tag{3.3}$$

where the last equality follows from continuity of u^r. This allows us to write the unknown coefficient functions as

$$a(t) = -\frac{1}{m}\frac{\mathrm{d}^2 X^r}{\mathrm{d}t^2} \qquad \text{and} \qquad b(t) = \frac{1}{m+1}\frac{\mathrm{d}^2 X^r}{\mathrm{d}t^2},$$

after which the pressure jump (3.1f) may be expressed as

$$[\![\hat{p}]\!] = b(t) - a(t) = -K(t)(m-1)(m+2)X^r(t). \tag{3.4}$$

We then have the following equation for the membrane location

$$\frac{\mathrm{d}^2 X^r}{\mathrm{d}t^2} + \widetilde{\omega}^2(1 + 2\tau \sin t)X^r = 0, \tag{3.5}$$

where

$$\widetilde{\omega}^2 = \frac{\kappa m(m-1)(m+1)(m+2)}{2m+1}.$$

Recalling the definition of κ in (2.11), we may write $\widetilde{\omega} = \omega_N/\omega$ as the ratio of the natural frequency ω_N for the unforced problem to the forcing frequency ω, where

$$\omega_N^2 = \frac{\sigma m(m-1)(m+1)(m+2)}{\rho R^3(2m+1)}. \tag{3.6}$$

This natural oscillation frequency ω_N corresponds to the classical result of Lamb [25, Art. 253] for oscillations of a spherical liquid drop, with the only difference being that a surface tension force replaces the elastic restoring force in our IB context.

We now focus on (3.5) which describes a harmonic oscillator with a time-dependent frequency parameter, and hence takes the form of the well-known Mathieu equation [29]. We invoke Floquet theory and look for a series solution of the form

$$X^r(t) = e^{\gamma t} \sum_{n=-\infty}^{\infty} X_n^r e^{\mathrm{i}nt},$$

where $\gamma \in \mathbb{C}$ is the Floquet exponent that determines the stability of solution as $t \to \infty$. Substituting this series expansion into (3.5) yields the following infinite system of linear algebraic equations:

$$-\mathrm{i}\left(\frac{(\gamma + \mathrm{i}n)^2}{\widetilde{\omega}^2} + 1\right) X_n^r = \tau(X_{n-1}^r - X_{n+1}^r) \qquad \text{for } n \in \mathbb{Z}. \tag{3.7}$$

Our aim is now to investigate all nontrivial solutions of (3.7) and determine what (if any) instabilities arise, and for which parameter values they occur. To this end, we use the standard approach and restrict ourselves to periodic solutions having $\mathrm{Re}\{\gamma\} = 0$ (i.e., neutral stability) and corresponding in particular to two special values of the Floquet exponent: $\gamma = 0$ (harmonic modes) and $\gamma = \frac{1}{2}\mathrm{i}$ (subharmonic modes). It is possible to show that all other values of $\mathrm{Im}\{\gamma\}$ give rise to modes that decay in time. To ensure that the resulting solutions are real-valued functions, we impose *reality conditions* on the Fourier series coefficients, which for the harmonic case are

$$X_{-n}^r = \overline{X}_n^r, \tag{3.8}$$

whereas for the subharmonic case

$$X_{-n}^r = \overline{X}_{n-1}^r, \tag{3.9}$$

for all $n \in \mathbb{Z}$. Either set of reality conditions implies that it is only necessary to consider nonnegative values of n, and so the linear system (3.7) may be written as

$$A_n X_n^r = \tau(X_{n-1}^r - X_{n+1}^r), \tag{3.10}$$

for $n = 0, 1, 2, \ldots$. Here, we treat the forcing amplitude τ as an unknown, and we approximate this infinite linear system by truncating at a finite number of modes N. The resulting equations may be written compactly in matrix form as

$$A\boldsymbol{v} = \tau B\boldsymbol{v}, \tag{3.11}$$

where and the unknown series coefficients are collected together in a vector

$$\boldsymbol{v} = \left[\ldots, \mathrm{Re}\{X_n^r\}, \mathrm{Im}\{X_n^r\}, \ldots\right]^T,$$

and $A = \mathrm{diag}(A_0, A_1, \ldots, A_N)$ is a block diagonal matrix with 2×2 blocks

$$A_n = \begin{bmatrix} \mathrm{Re}\{A_n\} & -\mathrm{Im}\{A_n\} \\ \mathrm{Im}\{A_n\} & \mathrm{Re}\{A_n\} \end{bmatrix}.$$

Similarly, B has a block tridiagonal structure of the form

$$B = \begin{bmatrix} \widehat{B} & \widetilde{B} & & & \\ I_2 & 0_2 & -I_2 & & \\ & I_2 & 0_2 & -I_2 & \\ & & \ddots & \ddots & \ddots \end{bmatrix},$$

where 0_2 and I_2 denote the 2×2 zero and identity matrices respectively. The sub-matrices making up the first block rows of A and B depend on γ, so that for the harmonic case (with $\gamma = 0$)

$$A_0 = I_2, \qquad \widehat{B} = 0_2, \qquad \widetilde{B} = \begin{bmatrix} 0 & 2 \\ 0 & 0 \end{bmatrix},$$

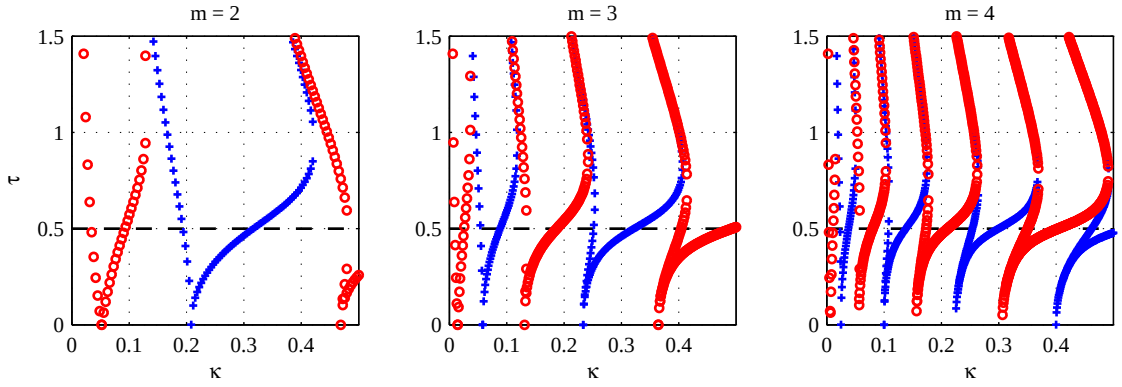

FIG. 3. *Ince-Strutt diagrams for the inviscid problem, showing stability contours for spherical harmonics $m = 2$ (left), 3 (center) and 4 (right). Subharmonic modes are denoted with ◯ and harmonic modes with +, and only modes with $\tau < \frac{1}{2}$ are physically relevant.*

whereas for the subharmonic case (with $\gamma = \frac{1}{2}\mathrm{i}$)

$$A_0 = \begin{bmatrix} \mathrm{Re}\{A_0\} & -\mathrm{Im}\{A_0\} \\ \mathrm{Im}\{A_0\} & \mathrm{Re}\{A_0\} \end{bmatrix}, \qquad \widehat{B} = \begin{bmatrix} 1 & 0 \\ 0 & -1 \end{bmatrix}, \qquad \widetilde{B} = -I_2.$$

Equation (3.10) can be viewed as a generalized eigenvalue problem with eigenvalue τ and eigenvector $\boldsymbol{v}$. Therefore, determining the stability of a parametrically-forced spherical membrane reduces to finding all values of τ and $\boldsymbol{v}$ for the two Floquet exponents $\gamma = 0$ and $\frac{1}{2}\mathrm{i}$, corresponding to the harmonic and subharmonic cases respectively.

A particularly effective way of visualizing these solutions is to vary one of the system parameters (e.g., forcing frequency or elastic stiffness) and to consider the *stability regions* that are generated as the eigenvalues trace out curves in parameter space. The resulting plot is referred to as an *Ince-Strutt diagram* [29], three of which are depicted in figure 3 as three plots of κ versus τ for the spherical harmonics $m = 2$, 3 and 4. The stability boundaries take the form of *fingers* or *tongues* that extend downward, and there are clearly two distinct sets of alternating fingers corresponding to harmonic and subharmonic modes, which we denote using points + and ◯ respectively. Parameter values lying above and inside any given finger correspond to unstable solutions, whereas all parameters lying below the fingers correspond to stable solutions. It is essential to keep in mind that only parameters lying below the horizontal line $\tau = \frac{1}{2}$ are physically relevant, since these values of τ correspond to a membrane stiffness $K(t)$ that remains positive.

It is evident from these diagrams that for a given forcing amplitude τ, an immersed spherical shell can experience parametric instability for a disjoint union of κ ranges (with corresponding ranges of the physical parameters ω, ρ, R and σ according to (2.11)). For example, different unstable modes (corresponding to different integer values of m) can be excited by forcing the system within a given range of ω. Furthermore, there are an infinitely many unstable modes that can be excited since the harmonic and subharmonic fingers alternate to the right *ad infinitum* as κ increases.

These membrane instabilities exist for forcing amplitudes satisfying $0 < \tau < \frac{1}{2}$ since each finger extends downward and touches the κ-axis as $\tau \to 0$. The points at which the fingers touch down correspond to the natural oscillation frequencies ω_N for the unforced problem given in (3.6). Indeed, we see that for $|\tau| \ll 1$, resonances occur at forcing frequencies $\omega_N = \frac{\ell}{2}\omega$ for any positive integer ℓ; that is, the natural frequency for a given m-mode is an integer multiple of half the parametric forcing frequency. A characteristic signature of parametric resonance is these subharmonic modes (odd ℓ) for which the response frequency is half of the forcing frequency.

4. Floquet analysis for a viscous fluid. Guided by the previous section, we apply Floquet theory to the original governing equations with viscosity, looking for series solutions of the form

$$\begin{aligned}
\boldsymbol{u}(r,\theta,\phi,t) &= e^{\gamma t}\sum_{n=-\infty}^{\infty} e^{\mathrm{i}nt}\left(u_n^r(r)\boldsymbol{Y}^c_{m,k} + u_n^{\Psi}(r)\boldsymbol{\Psi}^c_{m,k}\right),\\
\boldsymbol{X}(\xi,\eta,t) &= e^{\gamma t}\sum_{n=-\infty}^{\infty} e^{\mathrm{i}nt}\left(X_n^r\boldsymbol{Y}^c_{m,k} + X_n^{\Psi}\boldsymbol{\Psi}^c_{m,k}\right),\\
p(r,\theta,\phi,t) &= e^{\gamma t}\sum_{n=-\infty}^{\infty} e^{\mathrm{i}nt}p_n(r)Y^c_{m,k}.
\end{aligned}$$

The pressure coefficients $p_n(r)$ satisfy the same ODE (3.2) and boundedness conditions as in the inviscid case, and so the pressure has the same form

$$p_n(r) = \begin{cases} a_n r^m, & \text{if } r<1,\\ b_n r^{-m-1}, & \text{if } r>1,\end{cases}$$

with the only difference being that a_n and b_n are constants. Next, combining the radial momentum equation (2.28) with the divergence-free condition (2.31) and substituting the series form for u^r yields

$$r^2 u_n^{r\,\prime\prime} + 4r u_n^{r\,\prime} + \left(2 - m(m+1) - \beta_n^2 r^2\right)u_n^r - \frac{r^2}{\nu}\,p_n' = 0,$$

where primes denote derivatives with respect to the argument and

$$\beta_n = \sqrt{\frac{\gamma + \mathrm{i}n}{\nu}} \quad \text{with} \quad \mathrm{Re}\{\beta_n\} > 0.$$

We begin by considering the situation where $\beta_n \neq 0$, in which case the radial velocity can be expressed as

$$u_n^r(r) = \int_0^\infty \frac{z^2}{\nu}\,G(r,z)p_n'(z)\,\mathrm{d}z, \tag{4.1}$$

where $G(r,z)$ is the Green's function satisfying

$$r^2\frac{\partial^2 G}{\partial r^2} + 4r\frac{\partial G}{\partial r} + \left(2 - m(m+1) - \beta_n^2 r^2\right)G = \delta(r-z),$$

along with the two jump conditions

$$G\big|_{r=z^-}^{r=z^+} = 0 \qquad \text{and} \qquad r^2\frac{\partial G}{\partial r}\bigg|_{r=z^-}^{r=z^+} = 1.$$

The Green's function solution can be obtained explicitly as

$$G(r,z) = \begin{cases} z\beta_n h_m(\mathrm{i}\beta_n z)\,\dfrac{j_m(\mathrm{i}\beta_n r)}{r}, & \text{if } r<z,\\[2ex] z\beta_n j_m(\mathrm{i}\beta_n z)\,\dfrac{h_m(\mathrm{i}\beta_n r)}{r}, & \text{if } r>z,\end{cases}$$

where j_m and h_m denote mth-order spherical Bessel and Hankel functions of the first kind, respectively. The radial velocity in (4.1) may then be integrated explicitly to obtain

$$u_n^r(r) = \begin{cases} -\dfrac{\mathrm{i}j_m(\mathrm{i}\beta_n r)}{\nu r}\Big(m a_n h_{m+1}(\mathrm{i}\beta_n) - (m+1)b_n h_{m-1}(\mathrm{i}\beta_n)\Big) - \dfrac{m}{\nu\beta_n^2}a_n r^{m-1}, & \text{if } r<1,\\[2ex] -\dfrac{\mathrm{i}h_m(\mathrm{i}\beta_n r)}{\nu r}\Big(m a_n j_{m+1}(\mathrm{i}\beta_n) - (m+1)b_n j_{m-1}(\mathrm{i}\beta_n)\Big) + \dfrac{m+1}{\nu\beta_n^2}b_n r^{-m-2}, & \text{if } r>1.\end{cases}$$

The coefficients u_n^Ψ can be obtained by solving the incompressibility condition (2.31) for

$$u_n^\Psi(r) = \frac{1}{rm(m+1)}\frac{\mathrm{d}}{\mathrm{d}r}\left(r^2 u_n^r\right),$$
$$= \begin{cases} \left(-\dfrac{\mathrm{i}j_m(\mathrm{i}\beta_n r)}{\nu r} + \dfrac{\beta_n}{\nu} j_m'(\mathrm{i}\beta_n r)\right)\left(\dfrac{a_n h_{m+1}(\mathrm{i}\beta_n)}{m+1} - \dfrac{b_n h_{m-1}(\mathrm{i}\beta_n)}{m}\right) - \dfrac{a_n}{\nu\beta_n^2}\, r^{m-1}, & \text{if } r<1, \\ \left(-\dfrac{\mathrm{i}h_m(\mathrm{i}\beta_n r)}{\nu r} + \dfrac{\beta_n}{\nu} h_m'(\mathrm{i}\beta_n r)\right)\left(\dfrac{a_n j_{m+1}(\mathrm{i}\beta_n)}{m+1} - \dfrac{b_n j_{m-1}(\mathrm{i}\beta_n)}{m}\right) - \dfrac{b_n}{\nu\beta_n^2}\, r^{-m-2}, & \text{if } r>1. \end{cases}$$

The next major step is to determine values of the constants a_n and b_n by imposing the interface conditions (2.32). By orthogonality, the radial coefficients for membrane position satisfy

$$(\gamma + \mathrm{i}n)X_n^r = -\frac{\mathrm{i}a_n m}{\nu}\, h_m(\mathrm{i}\beta_n) j_{m+1}(\mathrm{i}\beta_n) + \frac{\mathrm{i}b_n(m+1)}{\nu}\, j_m(\mathrm{i}\beta_n) h_{m-1}(\mathrm{i}\beta_n),$$

with similar expressions holding for the other coefficients

$$(\gamma + \mathrm{i}n)X_n^\Psi = -\frac{\mathrm{i}a_n}{(m+1)\nu}\left(h_m(\mathrm{i}\beta_n) + \mathrm{i}\beta_n h_m'(\mathrm{i}\beta_n)\right) j_{m+1}(\mathrm{i}\beta_n) + \frac{\mathrm{i}b_n}{m\nu}\left(j_m(\mathrm{i}\beta_n) + \mathrm{i}\beta_n h_m'(\mathrm{i}\beta_n)\right) h_{m-1}(\mathrm{i}\beta_n).$$

These two equations may then be solved to obtain

$$a_n = -\frac{\mathrm{i}\nu^2\beta_n^3}{m}\,\frac{j_m(\mathrm{i}\beta_n) + \mathrm{i}\beta_n j_m'(\mathrm{i}\beta_n)}{j_{m+1}(\mathrm{i}\beta_n)}\, X_n^r + \mathrm{i}\nu^2\beta_n^3(m+1)\,\frac{j_m(\mathrm{i}\beta_n)}{j_{m+1}(\mathrm{i}\beta_n)}\, X_n^\Psi, \tag{4.2a}$$

$$b_n = -\frac{\mathrm{i}\nu^2\beta_n^3}{m+1}\,\frac{h_m(\mathrm{i}\beta_n) + \mathrm{i}\beta_n\, h_m'(\mathrm{i}\beta_n)}{h_{m-1}(\mathrm{i}\beta_n)}\, X_n^r + \mathrm{i}\nu^2\beta_n^3 m\,\frac{h_m(\mathrm{i}\beta_n)}{h_{m-1}(\mathrm{i}\beta_n)}\, X_n^\Psi, \tag{4.2b}$$

We are now prepared to impose the jump condition (2.26), which yields

$$\nu\left(-\frac{a_n}{m+1} - \frac{b_n}{m}\right) = \kappa(m-1)(m+2)\left(X_n^\Psi - \mathrm{i}\tau X_{n-1}^\Psi + \mathrm{i}\tau X_{n+1}^\Psi\right).$$

After replacing a_n and b_n in this equation with (4.2), we obtain the following linear equations relating coefficients X_n^r and X_n^Ψ:

$$\frac{\beta_n^3}{(m-1)(m+2)}\frac{\nu^2}{\kappa}\left(\frac{h_m(\mathrm{i}\beta_n)}{(m+1)h_{m-1}(\mathrm{i}\beta_n)} - \frac{j_m(\mathrm{i}\beta_n)}{m j_{m+1}(\mathrm{i}\beta_n)}\right) X_n^r + \left[\frac{\beta_n^3}{(m-1)(m+2)}\frac{\nu^2}{\kappa}\left(\frac{h_m(\mathrm{i}\beta_n)}{h_{m-1}(\mathrm{i}\beta_n)} + \frac{j_m(\mathrm{i}\beta_n)}{j_{m+1}(\mathrm{i}\beta_n)}\right) - \mathrm{i}\right] X_n^\Psi = \tau\left(X_{n-1}^\Psi - X_{n+1}^\Psi\right), \tag{4.3}$$

In a similar manner, the final jump condition (2.25) for pressure yields

$$\left[-\frac{\mathrm{i}\beta_n^4}{(2m+1)(m-1)(m+2)}\frac{\nu^2}{\kappa}\left(2 - \frac{m}{m+1}\frac{h_{m+1}(\mathrm{i}\beta_n)}{h_{m-1}(\mathrm{i}\beta_n)} - \frac{m+1}{m}\frac{j_{m-1}(\mathrm{i}\beta_n)}{j_{m+1}(\mathrm{i}\beta_n)}\right) - \mathrm{i}\right] X_n^r - \frac{\mathrm{i}\beta_n^4}{(2m+1)(m-1)(m+2)}\frac{\nu^2}{\kappa}\left(1 - m\frac{h_{m+1}(\mathrm{i}\beta_n)}{h_{m-1}(\mathrm{i}\beta_n)} + (m+1)\frac{j_{m-1}(\mathrm{i}\beta_n)}{j_{m+1}(\mathrm{i}\beta_n)}\right) X_n^\Psi = \tau\left(X_{n-1}^r - X_{n+1}^r\right). \tag{4.4}$$

Equations (4.3)–(4.4) represent a solvable system for X_n^r and X_n^Ψ in the case when $\beta_n \neq 0$.

We now consider the special case $\beta_n = 0$, which occurs only when $n = 0$ and $\gamma = 0$ (i.e., for harmonic modes) and the equation for radial velocity reduces to

$$r^2 u_0^{r\prime\prime} + 4r u_0^{r\prime} + \left(2 - m(m+1)\right) u_0^r - r^2\frac{p_0'}{\nu} = 0.$$

The corresponding Green's function is

$$G(r,z) = -\frac{1}{2m+1}\begin{cases} \dfrac{r^{m-1}}{z^m}, & \text{if } r < z, \\[2ex] \dfrac{z^{m+1}}{r^{m+2}}, & \text{if } r > z, \end{cases}$$

from which we obtain

$$u_0^r(r) = \begin{cases} a_0\dfrac{m}{\nu(2m+3)}r^{m+1} - \dfrac{1}{\nu(2m+1)}\left(a_0\dfrac{m}{2} - b_0\dfrac{m+1}{2m-1}\right)r^{m-1}, & \text{if } r < 1, \\[2ex] b_0\dfrac{m+1}{\nu(2m-1)}r^{-m} - \dfrac{1}{\nu(2m+1)}\left(a_0\dfrac{m}{2m+3} + b_0\dfrac{m+1}{2}\right)r^{-m-2}, & \text{if } r > 1. \end{cases}$$

Using the incompressibility condition as before, we find that

$$u_0^\Psi(r) = \begin{cases} a_0\dfrac{m+3}{\nu(2m+3)(m+1)}\,r^{m+1} - \dfrac{1}{\nu m(2m+1)}\left(a_0\dfrac{m}{2} - b_0\dfrac{m+1}{2m-1}\right)r^{m-1}, & \text{if } r < 1, \\[2ex] -b_0\dfrac{m-1}{\nu m(2m-1)}\,r^{-m} + \dfrac{1}{\nu(m+1)(2m+1)}\left(a_0\dfrac{m}{2m+3} + b_0\dfrac{m+1}{2}\right)r^{-m-2}, & \text{if } r > 1. \end{cases}$$

To ensure continuity across the membrane, we must have $a_0 = b_0 = 0$. Therefore, when $\beta_n = 0$ the jump conditions (2.25)–(2.26) reduce to

$$X_n^r - \mathrm{i}\tau X_{n-1}^r + \mathrm{i}\tau X_{n+1}^r = 0, \tag{4.5}$$

$$X_n^\Psi - \mathrm{i}\tau X_{n-1}^\Psi + \mathrm{i}\tau X_{n+1}^\Psi = 0. \tag{4.6}$$

The system of equations (4.3)–(4.6) can be written as

$$A_n X_n^r + B_n X_n^\Psi = \tau(X_{n-1}^r - X_{n+1}^r), \tag{4.7}$$

$$C_n X_n^r + D_n X_n^\Psi = \tau(X_{n-1}^\Psi - X_{n+1}^\Psi), \tag{4.8}$$

for suitably defined constants A_n, B_n, C_n and D_n. We again impose reality conditions for either harmonic solutions ($\gamma = 0$)

$$X_{-n}^r = \overline{X}_n^r \qquad \text{and} \qquad X_{-n}^\Psi = \overline{X}_n^\Psi, \tag{4.9}$$

or subharmonic solutions ($\gamma = \frac{1}{2}\mathrm{i}$)

$$X_{-n}^r = \overline{X}_{n-1}^r \qquad \text{and} \qquad X_{-n}^\Psi = \overline{X}_{n-1}^\Psi. \tag{4.10}$$

Again, we only need to consider nonnegative integer values of $n = 0, 1, \ldots, N$, so that equations (4.7)–(4.8) take the form of a generalized eigenvalue problem $A\boldsymbol{v} = \tau B\boldsymbol{v}$ with solution vector

$$\boldsymbol{v} = \big[\,\ldots,\, \mathrm{Re}\{X_n^r\},\, \mathrm{Im}\{X_n^r\},\, \mathrm{Re}\{X_n^\Psi\},\, \mathrm{Im}\{X_n^\Psi\},\ldots\big]^T.$$

of length $4(N+1)$. The matrix $A = \mathrm{diag}(A_0, A_1, \ldots, A_N)$ is block diagonal with 4×4 blocks

$$A_n = \begin{bmatrix} \mathrm{Re}\{A_n\} & -\mathrm{Im}\{A_n\} & \mathrm{Re}\{B_n\} & -\mathrm{Im}\{A_n\} \\ \mathrm{Im}\{A_n\} & \mathrm{Re}\{A_n\} & \mathrm{Im}\{B_n\} & \mathrm{Re}\{B_n\} \\ \mathrm{Re}\{C_n\} & -\mathrm{Im}\{C_n\} & \mathrm{Re}\{D_n\} & -\mathrm{Im}\{D_n\} \\ \mathrm{Im}\{C_n\} & \mathrm{Re}\{C_n\} & \mathrm{Im}\{D_n\} & \mathrm{Re}\{D_n\} \end{bmatrix},$$

and B is a block tridiagonal matrix of the form

$$B = \begin{bmatrix} \widehat{B} & \widetilde{B} & & & \\ I_4 & 0_4 & -I_4 & & \\ & I_4 & 0_4 & -I_4 & \\ & & \ddots & \ddots & \ddots \end{bmatrix},$$

where in the harmonic case

$$\widehat{B} = 0_4 \qquad \text{and} \qquad \widetilde{B} = \begin{bmatrix} 0 & 2 & 0 & 0 \\ 0 & 0 & 0 & 0 \\ 0 & 0 & 0 & 2 \\ 0 & 0 & 0 & 0 \end{bmatrix},$$

whereas in the subharmonic case

$$\widehat{B} = \begin{bmatrix} 1 & 0 & 0 & 0 \\ 0 & -1 & 0 & 0 \\ 0 & 0 & 1 & 0 \\ 0 & 0 & 0 & -1 \end{bmatrix} \qquad \text{and} \qquad \widetilde{B} = -I_4.$$

To study the stability of the viscous problem, we solve the eigenvalue equations for two values of dimensionless viscosity, $\nu = 10^{-3}$ and 6×10^{-3}, and take spherical harmonics numbered $m = 2, 3, 4$. In the numerical calculations, we use a truncation size of $N = 80$, since all coefficients $\{X_n^r, X_n^\Psi\}$ for $N > 80$ are less than 10^{-9} in magnitude and so can be easily neglected. The corresponding Ince-Strutt diagrams are shown in figure 4 where again we observe a well-defined sequence of alternating harmonic and subharmonic stability fingers in parameter space. These results reinforce one of the defining characteristics of parametric resonance, namely that such systems can experience instabilities leading to *unbounded growth* even in the presence of viscous damping.

There are few key comparisons to be drawn with the inviscid results from section 3. First of all, the stability fingers do not reach the κ-axis as they did in the inviscid case, but instead are deformed vertically upwards. As a result, there is a minimum forcing amplitude required to initiate resonance for any given value of κ. For the smaller value of viscosity $\nu = 10^{-3}$, fingers appear most similar to the inviscid case, while for larger ν the fingers deform upwards away from the κ-axis and shift outward to the right. Indeed, for large enough values of either viscosity or spherical harmonic m the fingers can lift entirely above the line $\tau = \frac{1}{2}$ so that resonant instabilities are no longer possible. This should be contrasted with the inviscid case where resonances exist for any value of m. We note that instabilities occur within the advective range (small ν, high Re) of the Navier-Stokes equations, however the initial perturbations are small enough that the solution is still within the linear (Stokes flow) regime.

The second distinction from the inviscid results is that within the nonphysical region $\tau > \frac{1}{2}$, an additional subharmonic solution appears as a curve of circular points cutting across the fingers. These unstable modes occur due to periodic modulation of the tangential stress across the membrane (2.27) and thus are not observed in the inviscid case. However, all of these modes are restricted to the nonphysical region $\tau > \frac{1}{2}$ and so they can be considered as spurious and safely ignored.

5. Numerical simulations. Our next aim is to verify the existence of parametric instabilities for an internally-forced spherical membrane using numerical simulations of the full governing equations (2.9). We use a parallel implementation of the IB algorithm by Wiens [41, 42] that utilizes a pseudo-compressible Navier-Stokes solver having particular advantages in terms of parallel speed-up on distributed clusters. The current implementation assumes a rectangular fluid domain with periodic boundary conditions, and we find that taking a cubic domain of side length $6R$ is sufficient to avoid any significant interference from adjacent periodic copies. The elastic shell is discretized using a triangulated mesh generated with the Matlab code `distmesh` [30], wherein each vertex is an IB node and each edge in the triangulation is a force-generating spring link joining adjacent nodes. The elastic force generated by the deformed membrane is simply the sum of all spring forces arising from the stretched spring network. The force density between any two IB nodes, say $\boldsymbol{X}_i$ and $\boldsymbol{X}_j$, has the form

$$\sigma^*\big(1 + 2\tau\sin(\omega t)\big)\big(\boldsymbol{X}_i - \boldsymbol{X}_j\big) \tag{5.1}$$

where σ^* is the spring constant that is not necessarily the same value as the membrane stiffness σ. It was shown in [20] that these two quantities are approximately related by

$$\sigma^* \approx \frac{\ln 3}{2}\sigma, \tag{5.2}$$

and so the spring constant must be scaled accordingly in order for the simulations to match the analytical results. The IB algorithm is formally second-order accurate in space, although a detailed convergence

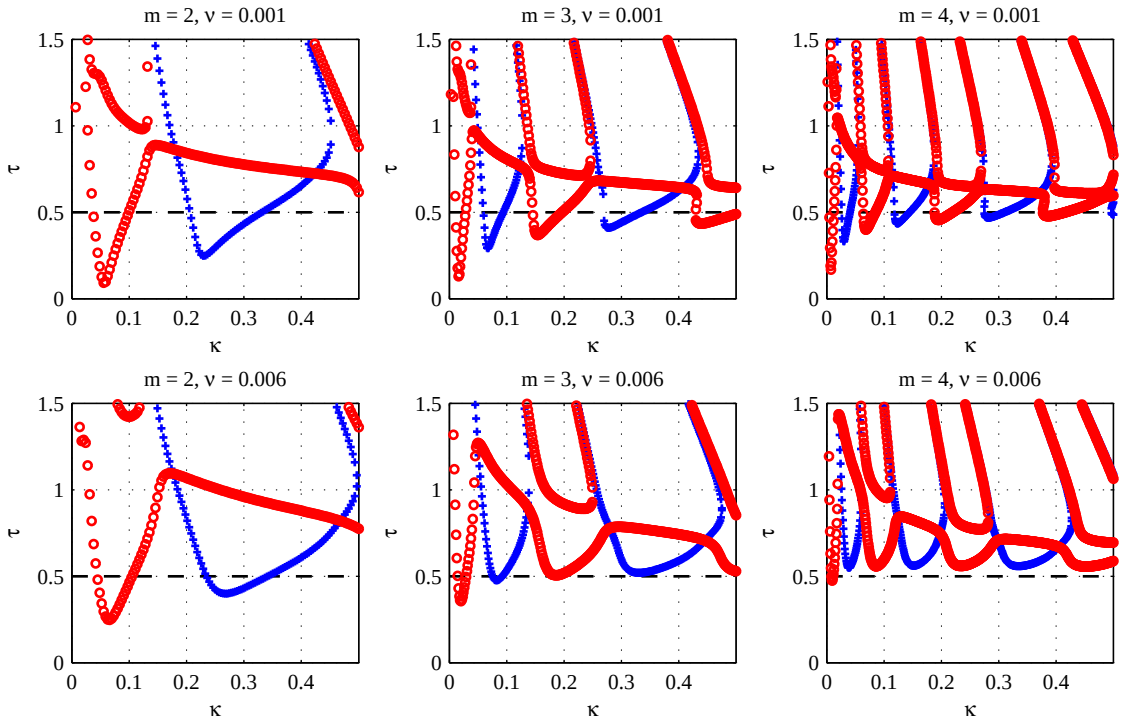

FIG. 4. *Ince-Strutt diagrams for the viscous problem with dimensionless viscosity* $\nu = 10^{-3}$ *(top) and* $\nu = 6 \times 10^{-3}$ *(bottom). Stability contours are shown for spherical harmonics* $m = 2$ *(left), 3 (center) and 4 (right). Subharmonic solutions are denoted with* ◯ *and harmonic solutions with* +.

study shows first-order convergence in the velocity $\boldsymbol{u}$ and IB position $\boldsymbol{X}$, and half-order convergence for pressure p owing to the discontinuity in pressure and velocity derivatives [41, 42]. Similar convergence rates are observed for an oscillating 3D spherical membrane.

In our simulations, the membrane is given an initial configuration

$$\boldsymbol{X}(\xi, \eta, 0) = R\big(1 + \epsilon Y^c_{m,k}(\xi, \eta)\big)\,\hat{r},$$

corresponding to a scalar spherical harmonic of degree m and order k with perturbation amplitude

$$\epsilon = \frac{0.05}{\max\limits_{\xi,\eta} \big|Y^c_{m,k}(\xi, \eta)\big|}\,.$$

We then performed numerical simulations for four different sets of parameters listed in table 1, which we refer to as cases 1–4. This table lists the physical parameters (ρ, μ, R, ω, σ) used in the simulations as well as the corresponding dimensionless parameters (ν, κ). The stability contours for each case 1–4 are shown in figure 5, this time in terms of plots of τ versus m, holding ν and κ fixed. This alternativee view of the stability regions allows us to identify unstable modes corresponding to physical oscillations, since it is only modes with integer m that are actually observable.

TABLE 1
Dimensionless and physical parameters for the four test cases.

Case	ν	κ	ρ (g/cm^3)	R (cm)	ω (1/s)	μ (g/cm s)	σ (g/s^2)
1	0.006	0.02	1	1	1	0.006	0.02
2	0.002	0.06	1	0.5	20	0.01	3
3	0.001	0.0075	1	0.5	20	0.005	0.375
4	0.004	0.25	1	10	0.05	0.02	0.625

Numerical simulations are performed by initializing the membrane with various (m,k)-modes lying inside and outside the highlighted unstable fingers so that direct comparisons can be drawn with our

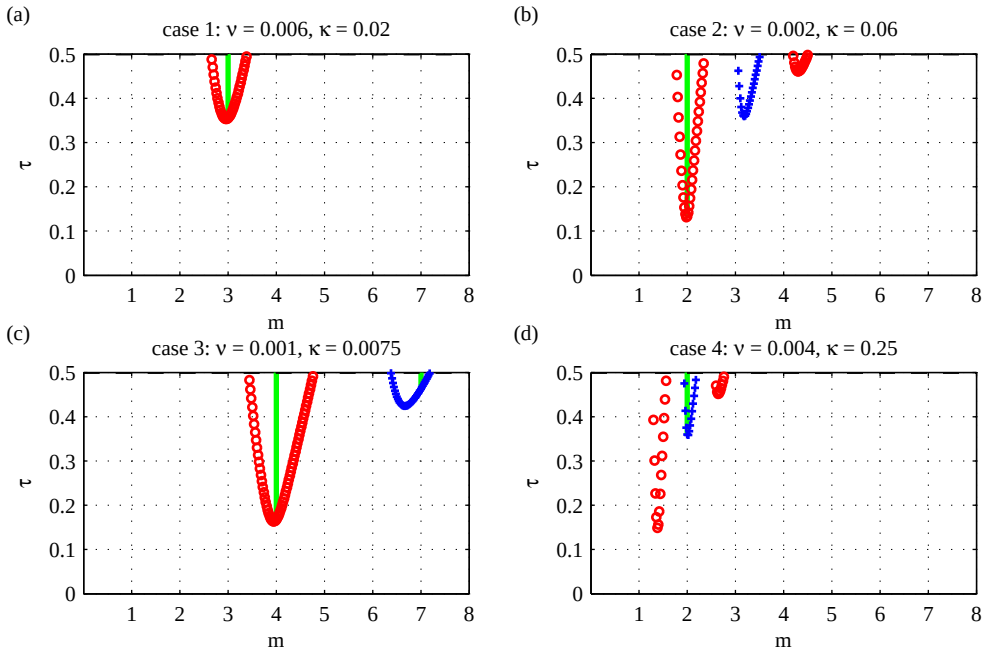

FIG. 5. *Ince-Strutt plots showing stability contours for each test case 1–4. Parameters that give rise to observable instabilities (i.e., corresponding to integer values of m) are highlighted by a vertical green line.*

analytical results. Figure 6 depicts several snapshots of the numerical solution for case 1, where the membrane was perturbed by a $(3,0)$-mode. The parametric forcing amplitude was set to $\tau = 0.45$,

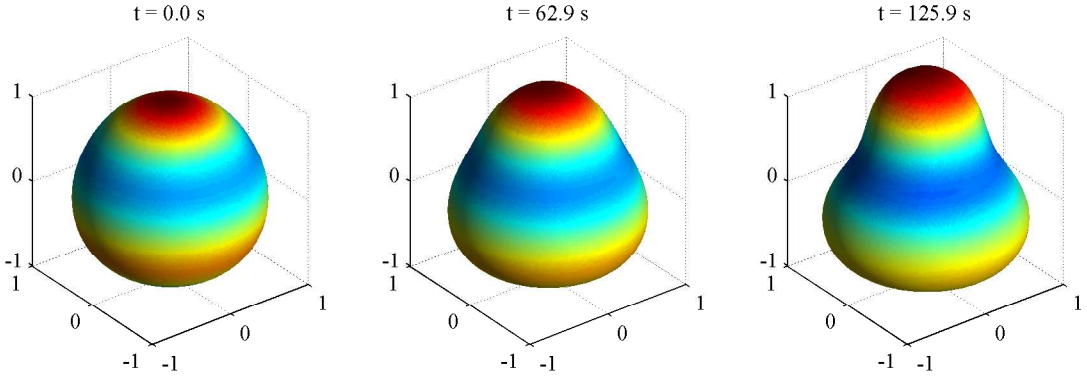

FIG. 6. *Several snapshots from the case 1 simulation where the membrane was initialized with a $(3,0)$-mode and the forcing amplitude is set to $\tau = 0.45$.*

which is well within the unstable finger in figure 5a. Over time, the small initial perturbation grows and oscillates with a frequency equal to one-half that of the forcing frequency, as expected from the linear analysis. To help visualize the growth of this mode over time, we compute the radial projection

$$X^r(t) = \int_0^{\pi}\int_0^{2\pi} \boldsymbol{X} \cdot \boldsymbol{Y}^c_{m,k} \sin\eta \, \mathrm{d}\xi \, \mathrm{d}\eta$$

at each time. This integral is computed by first interpolating the IB mesh values of $\boldsymbol{X}$ onto a regular (ξ,η) grid and then approximating the integral numerically using a Fast Fourier Transform in ξ and Gauss-Legendre quadrature in η. Figure 7 depicts the evolution of $X^r(t)$ for the $(3,0)$-mode, from which it is easy to see the expected period-doubling response to a waveform with period 4π. To illustrate that the membrane instability depends sensitively on the choice of mode m, figure 7 also shows simulations that were perturbed with $(2,0)$ and $(4,0)$-modes; in neither case is there any evidence of instability, which is also predicted by the stability plots in figure 5a.

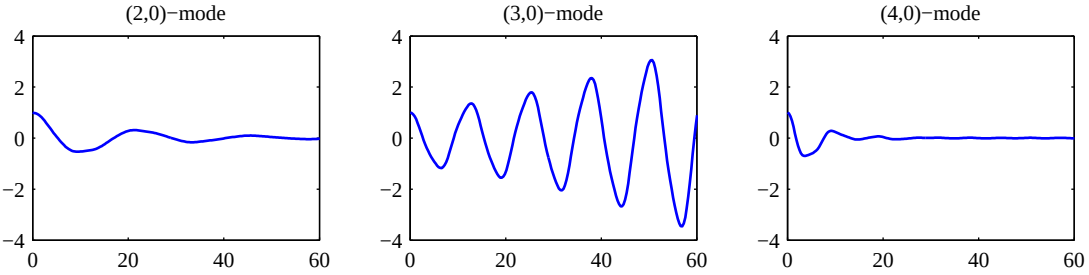

FIG. 7. *Simulated radial amplitude projection X^r for case 1. The shell is perturbed by three different (m, k)-modes, with $m = 3$ lying inside the unstable finger and $m = 2, 4$ outside. The solution is rescaled to start at $X^r = 1$.*

One conclusion of our analysis is that for each m, the stability of the linearized dynamics does not depend on the order k of the spherical harmonic. This property is illustrated in figure 8 as a plot of projected radial amplitude X^r for case 1 with two initial membrane shapes corresponding to modes $(3, 0)$ and $(3, 1)$. The analytical solution is provided for comparison, which we observe is nearly indistinguishable from the computed solution at early times. However, over time the perturbations grow and nonlinear effects take effect in the simulations, so that the growth rates eventually deviate from the linear analysis.

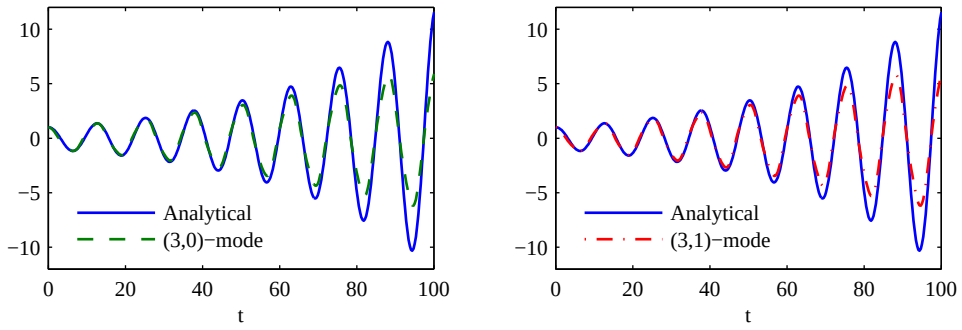

FIG. 8. *Radial amplitude projection X^r in case 1, showing a spherical shell perturbed by a $(3, 0)$-mode (left, dashed) and a $(3, 1)$-mode (right, dash-dot). The exact result from the linear analysis is shown as a solid line. All curves are rescaled to start at $X^r = 1$.*

As another illustration of the impact of parameters on stability, we perform a series of simulations to investigate the "sharpness" of the stability fingers. Using parameters from case 2, we fix $\tau = 0.25$ and then investigate the behavior of the numerical solution as κ is varied. Based on figure 5b, we expect case 2 to be unstable if the membrane configuration is an $m = 2$ mode but that slight a change in the parameters can stabilize the 2-mode. Figure 9a shows the Ince-Strutt diagram as a plot of τ versus κ for $\nu = 0.002$ and $m = 2$. The parameter values used in this series of tests are denoted by $\triangle$ in figure 9a, with the center point in the middle of the subharmonic finger corresponding to case 2, and the remaining parameters lying close to the stability boundary ($\kappa \approx 0.048$ and 0.074) or else just outside. Figures 9b–f depict the radial projection X^r for each of these five simulations, from which we observe that as κ increases the solution transitions from stable to unstable and back to stable again. The computed stability boundaries do not correspond exactly with the analytical results, especially the upper stability limit $\kappa \approx 0.074$; nonetheless, the match is reasonable considering that the analysis is linear.

Finally, we show in figure 10 plots of the radial amplitude projection for cases 1–4, in which the spherical shell is perturbed by a mode that we know from the analysis to be unstable. The forcing amplitude is set to $\tau = 0.45$ in all cases. Snapshots of the membrane evolution are provided for each simulation to illustrate the growth of the given modes. All simulations exhibit the expected unstable growth in solution amplitude, although we stress that the numerical results do not lead to unbounded growth in amplitude as suggested by the linear analysis. We attribute this discrepancy in behavior to nonlinear effects that become important later in the simulation and limit solution growth once

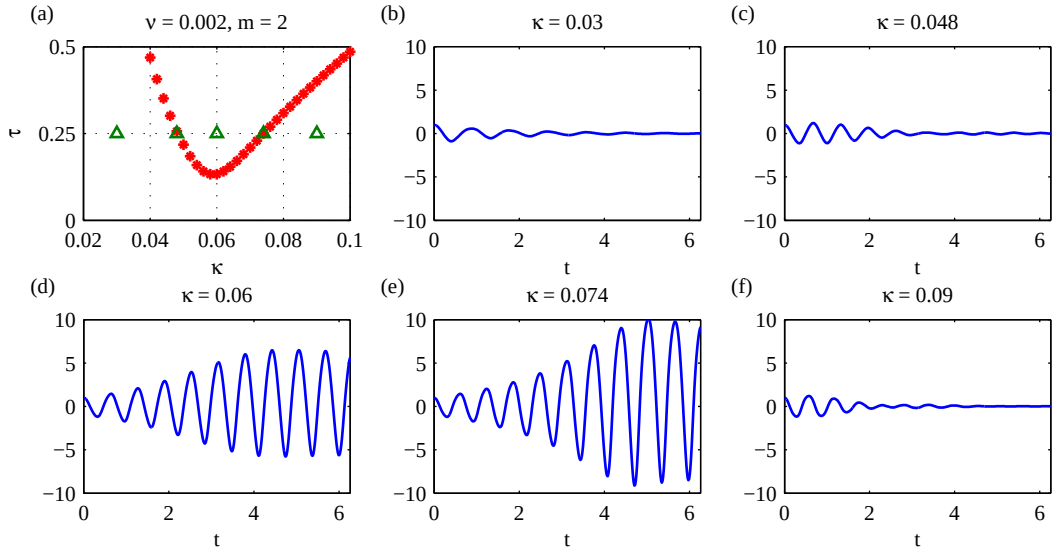

FIG. 9. *(a) Ince-Strutt diagram for $m = 2$ and $\nu = 0.002$ but with varying κ. The parameters used are denoted by $\triangle$, with the center point corresponding to case 2. (b)–(f) Radial projection from simulations for a range of κ values. The membrane was initialized with a $(2, 0)$-mode and all curves are rescaled to start at $X^r = 1$.*

the amplitude of oscillations become large enough. We also note that the correct frequency response is observed in all four tests, with cases 1–3 exhibiting the expected period-doubling subharmonic response, while case 4 oscillates with a harmonic response.

6. FSI benchmark problem. An oscillating spherical shell is a common test problem used to test numerical methods for FSI problems [8, 11, 34]. However, to our knowledge there is as yet no well-established benchmark. We therefore propose a simple FSI benchmark problem for an internally-forced elastic membrane to which computational scientists can compare their simulations. The parameters for the benchmark problem are listed in table 2 and the membrane is perturbed with a $(3, 0)$-mode

$$\boldsymbol{X}(\xi, \eta, 0) = R\left(1 + 0.05\left(\frac{5}{2}\cos^3\eta - \frac{3}{2}\cos\eta\right)\right)\hat{\boldsymbol{r}}(\xi, \eta). \tag{6.1}$$

We note that these parameters and initial configuration result in a resonant subharmonic mode and so the simulation covers two oscillation periods. To provide a simple means to compare results, we list in table 3 the largest distance from the membrane to the equilibrium state at each half-period for both analytical and simulated results. We also list results from an unforced simulation by setting $\tau = 0$ and holding all other parameters the same. Data files from our simulation are included as supplementary material.

TABLE 2
Parameters for the FSI benchmark problem.

fluid density	$\rho = 1.0$ g/cm^3
fluid viscosity	$\mu = 0.01$ g/s cm
membrane stiffness	$\sigma = 0.1$ g/s^2
membrane rest radius	$R = 0.5$ cm
forcing frequency	$\omega = 2\pi$ 1/s
forcing amplitude	$\tau = 0.45$
computational domain	$\Omega = [-1, 1]^3$
grid resolution	$\Delta x = 1/32$
time step	$\Delta t = 1.25 \times 10^{-4}$
final time	$t_{\text{final}} = 4$ s

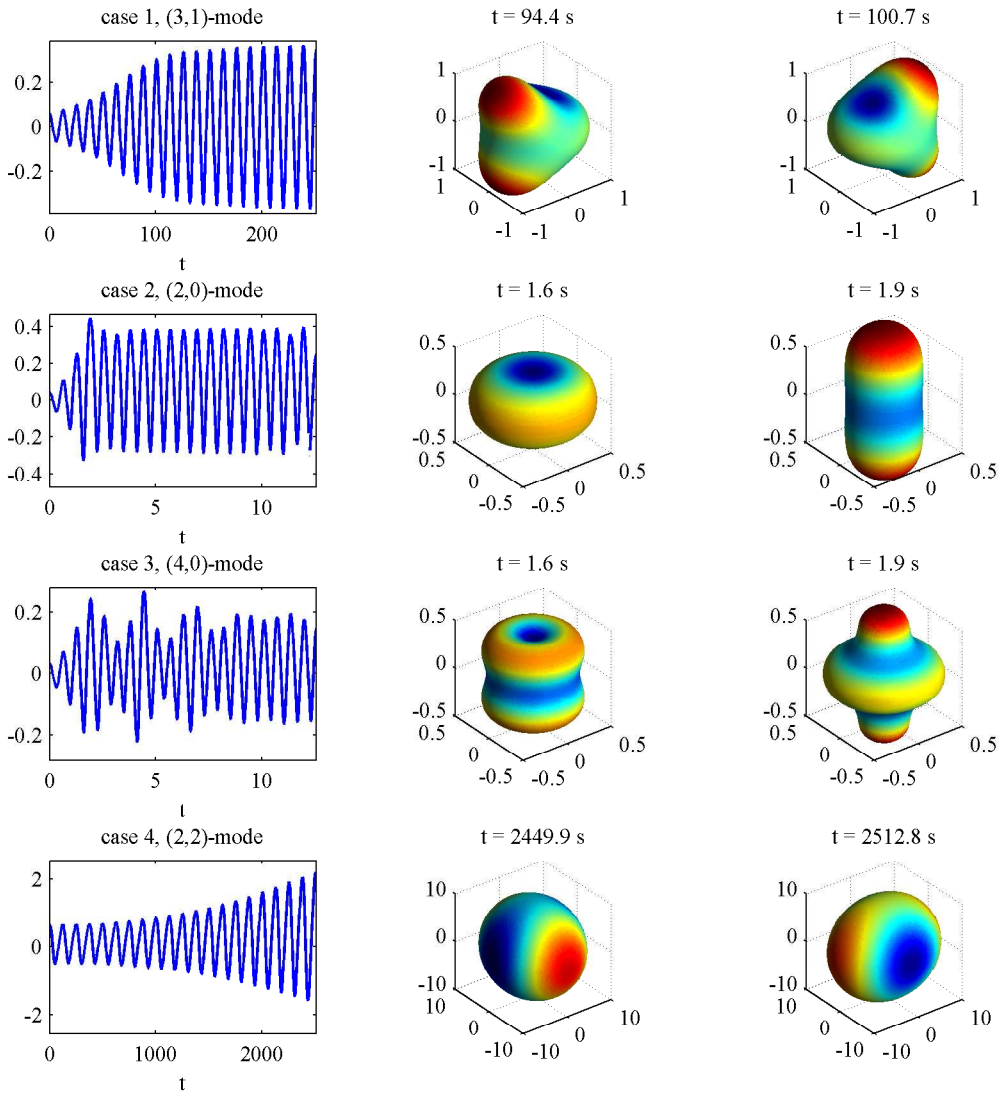

FIG. 10. *Simulation results for cases 1–4 with the spherical shell perturbed by a mode that is expected to be unstable, with* $\tau = 0.45$. *The left column shows the radial projection* X^r *and snapshots from the corresponding simulations are shown on the right.*

TABLE 3

Largest extent of the membrane from the equilibrium state (in cm) at each half-period for forced and unforced cases. Both analytical and numerical results are shown for comparison.

Forced membrane ($\tau = 0.45$)

	$t = 0$	$t = 1$	$t = 2$	$t = 3$	$t = 4$
analytical	0.02500	0.02835	0.03216	0.03647	0.04136
numerical	0.02499	0.03136	0.03265	0.03765	0.04318

Unforced membrane ($\tau = 0$)

	$t = 0$	$t = 0.9745$	$t = 1.949$	$t = 2.9235$	$t = 3.898$
analytical	0.02500	0.01352	0.007316	0.003957	0.002141
numerical	0.02499	0.01597	0.007751	0.003412	0.002495

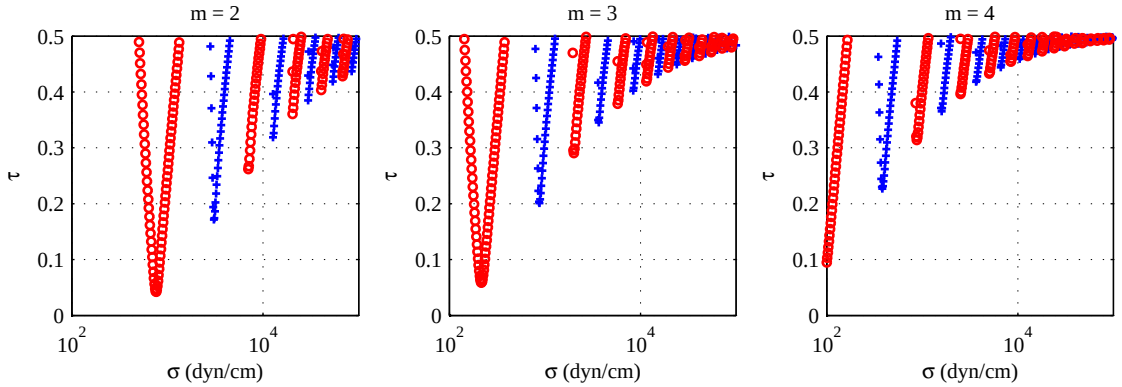

FIG. 11. *Stability contours for physical parameters corresponding to a human heart undergoing an abnormal heart rhythm ($\nu = 2.39 \times 10^{-4}$) for modes $m = 2$ (left), 3 (center) and 4 (right).*

7. Application to the heart and other biofluid systems. Our work on parametric forcing in immersed elastic shells was originally motivated by the study of actively-beating heart muscle fibers that interact with surrounding blood and tissue. Heart muscle contractions are initiated by complex waves of electrical signals that propagate through the heart wall, which should be contrasted with the spatially-uniform coordinated contractions analyzed in this paper. Furthermore, heart chambers have an irregular shape and a thick wall that depart significantly from a spherical shell of zero thickness. Nonetheless, it is natural to ask whether our analysis of spherical immersed elastic shells with a periodic internal forcing could still yield any useful insights into the nature of the complex fluid-structure interaction between a beating heart and the surrounding fluid.

To this end, we consider an immersed spherical shell with parameters approximating a human heart under two conditions: first, a normal healthy heart; and second, an abnormal heart undergoing a much faster heartbeat. We then ask whether our analysis suggests resonant behavior in either case for physiologically relevant heart beat frequencies. There is a wide range of abnormal heart rhythms classified as *supraventricular tachycardias* or SVTs [27, 33] that correspond to a heart beat that is either irregular or abnormally rapid and which occurs in the heart's upper chambers (called the left and right atria). In contrast with ventricular tachycardias, which are much more dangerous, many SVTs are non-life-threatening and can persist for long periods of time. Therefore, we will focus on SVTs (in the atria) where fluid dynamic instabilities are more likely to have the time to develop.

We now discuss an appropriate choice of parameters for an IB model of FSI in the heart. The resting heart rate for a healthy person ranges from 60–100 beats per minute (bpm) and both atria and ventricles beat in synchrony. In contrast, a heart characterized by SVT can exhibit two separate beats in the atria and ventricles, with an atrial rhythm lying anywhere between 100–600 bpm. A clinical study by [39] surveyed 322 patients suffering from atrial fibrillation (one sub-class of SVT) and obtained measurements of atrial wall stiffness σ varying between 1×10^3 and 2×10^4 dyn/cm. We have found no evidence to suggest that stiffness varies significantly between hearts with normal and abnormal rhythms, and so we use the same range of σ for all cases. Although hearts suffering from conditions such as atrial fibrillation are often characterized by increased size [39], we elect to use a single representative value of radius $R = 2.0$ cm for an atrium in both normal and diseased hearts. In terms of fluid properties, blood has density similar to water with $\rho = 1$ g/cm^3 but has a significantly higher dynamic viscosity of $\mu = 0.04$ g/cm s. We choose a representative SVT rhythm with frequency $\omega = 400$ bpm, which translates into a dimensionless viscosity parameter $\nu = 2.39 \times 10^{-4}$.

After substituting these parameter values into our analytical results from section 4 for modes numbered $m = 2, 3, 4$, we obtain the Ince-Strutt plots in figure 11. The stability fingers are depicted with the elastic stiffness parameter σ plotted along the horizontal axis, and the results show that parametric instabilities can arise for most values of σ under consideration. Because resonant instabilities occur over such a wide range of stiffness corresponding to measurements in the left atrium [39], it seems reasonable to hypothesize that FSI-driven parametric instability may influence the dynamics of the beating heart.

We now delve further into the stability plots of figure 11 and remark that experiments suggest heart muscle is seldom (if ever) completely slack; therefore, we expect that the forcing amplitude τ

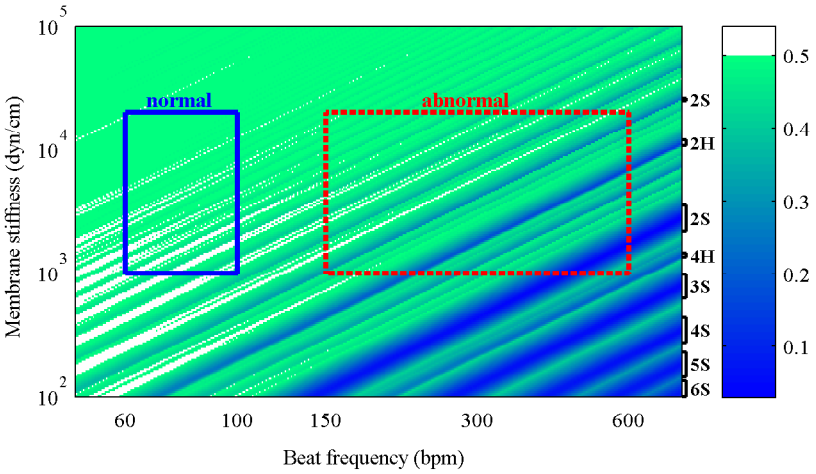

FIG. 12. *Minimum value of τ required for parametric resonance across modes 2–6. White areas represent parameters for which no physical instability exists. Each dark (blue) band is labeled by its corresponding unstable m-mode and response frequency ('H' for harmonic or 'S' for subharmonic). The boxes indicate parameter ranges for a healthy heart (solid, blue) and for a heart with SVT (dashed, red).*

lies significantly below the threshold value of $\frac{1}{2}$. Indeed, an estimate of $\tau \approx 0.3$ can be extracted from measurements of pressure in the left atrium taken by Braunwald et al. [4, Fig. 1]. Figure 12 provides an alternate view of the dependence of resonant instabilities on parameters by depicting the minimum τ giving rise to resonance as a function of elastic stiffness and beat frequency (taking modes $m = 2, \ldots, 6$). We are especially interested in the dark (blue) bands that correspond to smaller values of τ and hence more prominent instabilities. Taking a value of $\tau = 0.3$, our analysis predicts "valleys" of instability corresponding to discrete ranges of the parameters ω and σ. For fixed σ, we observe that at low frequency the valleys are very narrow and steep, while as the forcing frequency increases the width of the unstable bands likewise increases. In particular, if we consider an intermediate value of σ for a "normal" heart beating at 60–100 bpm, then the unstable bands are relatively small and so resonances would seem less likely. On the other hand, if the frequency is increased to 300–600 bpm then we begin to encounter wider valleys that suggest instabilities for a smaller value of τ.

In summary, we found that resonant instabilities are possible for a wide range of parameters corresponding to normal and abnormal hearts. Furthermore, at higher frequencies characteristic of SVT, instabilities are not only more likely to occur but also persist over wider ranges of parameter space. As suggestive as these results are, we refrain from making any specific claims or predictions regarding resonance in an actual beating heart because so many simplifications and assumptions have been made: our applied periodic forcing is oversimplified, nonlinearities are neglected, a spherical shell is a far cry from an atrium, and some parameter values remain uncertain. Nonetheless, the fact that our analysis predicts resonance over such a wide range of physiologically relevant parameters is compelling enough to suggest that this problem merits further investigation. Moreover, it should be possible to test for the presence of isolated parametric instabilities in carefully designed experiments, and our parameter study above provides guidance on what ranges of parameters are most worthy of investigating.

In addition to the heart, there are many other complex biofluid systems that undergo similar periodic internal forcing and to which our analysis could potentially be applied. Parametric forcing in spherical membranes occurs in the context of dielectric characterization and manipulation of biological cells (erythrocytes and lymphocytes) by way of an applied electric field [43]. Another such problem was considered by Cottet and Maitre [9], who were motivated by the study of cell membrane protrusions appearing during cell locomotion. A much simpler geometry in which we have already applied a similar Floquet analysis is an IB model for the basilar membrane in the inner ear [21]. This problem involved a flat membrane for which the Floquet expansion takes a much simpler form in terms of trigonometric eigenfunctions, and we provided evidence that parametric resonance could play a role in the astounding ability of the mammalian ear to sense and process sound.

Another common geometry that is intermediate in complexity between a flat membrane and spherical shell is a cylindrical tube, which features prominently in many biological applications and engineering

systems. Indeed, there are many examples of FSI systems involving flow through a compliant cylindrical tube wherein some form of periodic forcing is known to induce resonance, including blood flow through artery-organ systems [40], air flow-induced vibrations of the bronchi [12], and the resonant impedance pump [2, 28] whose design was incidentally inspired by observations of resonant pumping in the embryonic heart. Another exciting avenue for future work is to extend our Floquet analysis to a cylindrical shell, which could provide new insight into resonant instabilities arising in these other FSI systems. One advantageous side-effect of studying this cylindrical geometry is that it avoids the complexity of vector spherical harmonics and instead employs a simpler Floquet series solution consisting of Fourier-Bessel eigenfunctions, similar to the 2D radial solution obtained for a circular membrane in [6].

8. Conclusions. In this paper, we demonstrated the existence of parametric instabilities in a spherical elastic shell immersed in an incompressible viscous fluid, wherein the motion is driven by periodic contractions of the shell. A mathematical model was derived using an immersed boundary framework that captures the full two-way interaction between the elastic material and surrounding fluid. A Floquet analysis of the linearized governing equations is performed using an expansion in terms of vector spherical harmonics. We obtained results regarding the stability of the internally forced system with and without viscosity, and showed with the aid of Ince-Strutt diagrams that fluid-mechanical resonance exists regardless of whether viscous damping is present. Numerical simulations of the full IB model were performed that confirm the presence of these parametric resonances. In parallel with this work, we have initiated an experimental study of rubber water balloons immersed in water [22] in which we measure the natural modes of oscillation of these immersed (nearly-spherical) membranes and use the results to validate our analytical predictions.

Because our original motivation for considering this problem derived from the study of periodic contractions driving blood flow in the heart, we also discussed the relevance of our stability analysis to cardiac fluid dynamics. Indeed, our analysis suggests that periodic resonance can occur in an idealized spherical shell geometry for physical parameters corresponding to the heart, and provides possible parameter ranges to focus on for an experimental study designed to test for the existence of resonant solutions. These results are preliminary and much more work needs to be done to determine whether fluid-structure driven resonances could actually play a meaningful role in cardiac flows.

One major step in bringing our results closer to the actual heart is to generalize our time-periodic and spatially uniform driving force to include the effect of spiral waves of contraction that are initiated through electrical signals propagating in the heart wall. Including such spatiotemporal variations in the driving force would naturally couple together the radial and angular solution components. As a result, we would then lose the special advantage we gained from our choice of vector spherical harmonics that led to a fortunate mode-decoupling in the interfacial jump conditions. Generalizing the analysis to handle this fully coupled problem would require considerable effort, but could lead to significant new insights into a more realistic model of FSI in the beating heart.

Acknowledgments. We thanks Jeffrey Wiens for permitting us to use his immersed boundary code, as well as for providing assistance with the numerical simulations.

REFERENCES

[1] M. Abramowitz and I. A. Stegun, *Handbook of Mathematical Functions With Formulas, Graphs and Mathematical Tables*, Dover Publications, New York, 1965.
[2] I. Avrahami and M. Gharib, *Computational studies of resonance wave pumping in compliant tubes*, J. Fluid Mech., 608 (2008), pp. 139–160.
[3] R. Barrera, G. Estevez, and J. Giraldo, *Vector spherical harmonics and their application to magnetostatics*, Euro. J. Phys., 6 (1985), pp. 287–294.
[4] E. Braunwald, E. C. Brockenbrough, C. J. Frahm, and J. Ross, Jr., *Left atrial and left ventricular pressures in subjects without cardiovascular disease: Observations in eighteen patients studied by transseptal left heart catheterization*, Circulation, 24 (1961), pp. 267–269.
[5] A. R. Champneys, *The dynamics of parametric excitation*, in Encyclopedia of Complexity and Systems Science, Robert A. Meyers, ed., Springer, 2009, pp. 2323–2344.
[6] R. Cortez, C. S. Peskin, J. M. Stockie, and D. Varela, *Parametric resonance in immersed elastic boundaries*, SIAM J. Appl. Math., 65 (2004), pp. 494–520.
[7] R. Cortez and D. Varela, *The dynamics of an elastic membrane using the impulse method*, J. Comput. Phys., 138 (1997), pp. 224–247.
[8] G. Cottet and E. Maitre, *A level set method for fluid-structure interactions with immersed surfaces*, Math. Models Meth. Appl. Sci., 16 (2006), pp. 415–438.

[9] G. Cottet, E. Maitre, and T. Milcent, *An Eulerian method for fluid-structure coupling with biophysical applications*, in Proc. Euro. Conf. Comput. Fluid Dyn. (ECCOMAS CFD 2006), P. Wesseling, E. Oñate, and J. Périaux, eds., Egmond aan Zee, The Netherlands, Sept. 5–8, 2006.
[10] B. U. Felderhof, *Jittery velocity relaxation of an elastic sphere immersed in a viscous incompressible fluid*, Phys. Rev. E, 89 (2014), p. 033001.
[11] E. Givelberg, *Modeling elastic shells immersed in fluid*, Commun. Pure Appl. Math., 57 (2004), pp. 283–330.
[12] J. B. Grotberg, *Pulmonary flow and transport phenomena*, Annu. Rev. Fluid Mech., 26 (1994), pp. 529–571.
[13] A. Y. Gunawan, J. Molenaar, and A. A. F. van de Ven, *Does shear flow stabilize an immersed thread?*, Euro. J. Mech. B, 24 (2005), pp. 379–396.
[14] W. W. Hansen, *A new type of expansion in radiation problems*, Phys. Rev., 47 (1935), pp. 139–143.
[15] E. L. Hill, *The theory of vector spherical harmonics*, Amer. J. Phys., 22 (1954), p. 211.
[16] W. Huang and H. J. Sung, *An immersed boundary method for fluid–flexible structure interaction*, Comput. Meth. Appl. Mech. Eng., 198 (2009), pp. 2650–2661.
[17] R. W. James, *The spectral form of the magnetic induction equation*, Proc. R. Soc. London A, 340 (1974), pp. 287–299.
[18] R. E. Kelly, *The flow of a viscous fluid past a wall of infinite extent with time-dependent suction*, Quart. J. Mech. Appl. Math., 18 (1965), pp. 287–298.
[19] C. Kleinstreuer, *Biofluid Dynamics: Principles and Selected Applications*, CRC Press, Boca Raton, 2006.
[20] W. Ko, *Parametric resonance in immersed elastic structures, with application to the cochlea*, PhD thesis, Department of Mathematics, Simon Fraser University, May 2015.
[21] W. Ko and J. M. Stockie, *An immersed boundary model of the cochlea with parametric forcing*, SIAM J. Appl. Math. under revision.
[22] W. Ko, D. Tse, and J. M. Stockie, *Natural oscillations of a water balloon immersed in fluid*. In preparation, 2014.
[23] K. Kumar and L. S. Tuckerman, *Parametric instability of the interface between two fluids*, J. Fluid Mech., 279 (1994), pp. 49–68.
[24] M. Lai and Z. Li, *A remark on jump conditions for the three-dimensional Navier-Stokes equations involving an immersed moving membrane*, Appl. Math. Lett., 14 (2001), pp. 149–154.
[25] H. Lamb, *Hydrodynamics*, Cambridge University Press, 1932.
[26] Sir J. Lighthill, ed., *Mathematical Biofluiddynamics*, vol. 17 of CBMS-NSF Regional Conference Series in Applied Mathematics, SIAM, Philadelphia, 1975.
[27] M. S. Link, *Evaluation and initial treatment of supraventricular tachycardia*, New Engl. J. Med., 367 (2012), pp. 1438–1448.
[28] L. Loumes, I. Avrahami, and M. Gharib, *Resonant pumping in a multilayer impedance pump*, Phys. Fluids, 20 (2008), p. 023103.
[29] A. H. Nayfeh, *Introduction to Perturbation Techniques*, John Wiley & Sons, New York, 1993.
[30] P. Persson and G. Strang, *A simple mesh generator in Matlab*, SIAM Rev., 46 (2004), pp. 329–345.
[31] C. S. Peskin, *Numerical analysis of blood flow in the heart*, J. Comput. Phys., 25 (1977), pp. 220–252.
[32] ———, *The immersed boundary method*, Acta Numer., (2002), pp. 1–39.
[33] R. E. Phillips and M. K. Feeney, *The Cardiac Rhythms: A Systematic Approach to Interpretation*, Saunders, Philadelphia, PA, 1973.
[34] S. Ramanujan and C. Pozrikidis, *Deformation of liquid capsules enclosed by elastic membranes in simple shear flow: large deformations and the effect of fluid viscosities*, J. Fluid Mech., 361 (1998), pp. 117–143.
[35] C. Semler and M. P. Païdoussis, *Nonlinear analysis of the parametric resonances of a planar fluid-conveying cantilevered pipe*, J. Fluids Struct., 10 (1996), pp. 787–825.
[36] J. M. Stockie and B. T. R. Wetton, *Stability analysis for the immersed fiber problem*, SIAM J. Appl. Math., 55 (1995), pp. 1577–1591.
[37] D. Terzopoulos and K. Fleischer, *Deformable models*, Visual Computer, 4 (1988), pp. 306–331.
[38] S. Vogel, *Life in Moving Fluids: The Physical Biology of Flow*, Princeton University Press, second ed., 1994.
[39] W. Wang, D. Buehler, A. M. Martland, X. D. Feng, and Y. J. Wang, *Left atrial wall tension directly affects the restoration of sinus rhythm after Maze procedure*, Eur. J. Cardiothorac. Surg., 40 (2011), pp. 77–82.
[40] Y.-Y. L. Wang, M.-Y. Jan, C.-S. Shyu, C.-A. Chiang, and W.-K. Wang, *The natural frequencies of the arterial system and their relation to the heart rate*, IEEE Trans. Biomed. Eng., 51 (2004), pp. 193–195.
[41] J. K. Wiens, *An efficient parallel immersed boundary algorithm, with application to the suspension of flexible fibers*, PhD thesis, Department of Mathematics, Simon Fraser University, Aug. 2014.
[42] J. K. Wiens and J. M. Stockie, *An efficient parallel immersed boundary algorithm using a pseudo-compressible fluid solver*, J. Comput. Phys., 281 (2015), pp. 917–941.
[43] A. Zehe and A. Ramírez, *Vibration of eukariotic cells in suspension induced by a low-frequency electric field: A mathematical model*, Trans. Biol. Biomed., 1 (2004), pp. 55–59.